© ESO 2017

Chasing disks around O-type (proto)stars:
Evidence from ALMA observations

R. Cesaroni[1], Á. Sánchez-Monge[2], M. T. Beltrán[1], K. G. Johnston[3], L. T. Maud[4], L. Moscadelli[1], J. C. Mottram[5], A. Ahmadi[5], V. Allen[6], H. Beuther[5], T. Csengeri[7], S. Etoka[8], G. A. Fuller[9,10], D. Galli[1], R. Galván-Madrid[11], C. Goddi[12,4], T. Henning[5], M. G. Hoare[13], P. D. Klaassen[14], R. Kuiper[15], M. S. N. Kumar[16,17], S. Lumsden[18], T. Peters[19], V. M. Rivilla[1], P. Schilke[2], L. Testi[20,1], F. van der Tak[21,6], S. Vig[22], C. M. Walmsley[23,1], and H. Zinnecker[24]

[1] INAF, Osservatorio Astrofisico di Arcetri, Largo E. Fermi 5, I-50125 Firenze, Italy e-mail: cesa@arcetri.astro.it
[2] I. Physikalisches Institut, Universität zu Köln, Zülpicher Strasse 77, 50937, Köln, Germany
[3] School of Physics and Astronomy, University of Leeds, West Yorkshire, Leeds LS2 9JT, UK
[4] ALLEGRO/Leiden Observatory, Leiden University, PO Box 9513, NL-2300 RA Leiden, the Netherlands
[5] Max Planck Institute for Astronomy, Königstuhl 17, D-69117 Heidelberg, Germany
[6] Kapteyn Astronomical Institute, University of Groningen, 9700 AV, Groningen, The Netherlands
[7] Max-Planck-Institut für Radioastronomie, Auf dem Hügel 69, D-53121 Bonn, Germany
[8] Hamburger Sternwarte, Universität Hamburg, 21029, Hamburg, Germany
[9] Jodrell Bank Centre for Astrophysics, School of Physics and Astronomy, The University of Manchester, Oxford Road, Manchester M13 9PL, UK
[10] UK ALMA Regional Centre Node
[11] Instituto de Radioastronomía y Astrofísica, UNAM, Apdo. Postal 3-72 (Xangari), 58089 Morelia, Michoacán, México
[12] Department of Astrophysics/IMAPP, Radboud University, P.O. Box 9010, 6500 GL Nijmegen, The Netherlands
[13] School of Physics and Astronomy, University of Leeds, Leeds LS2 9JT, UK
[14] UK Astronomy Technology Centre, Royal Observatory Edinburgh, Blackford Hill, Edinburgh EH9 3HJ, UK
[15] Institut für Astronomie und Astrophysik, Universität Tübingen, Auf der Morgenstelle 10, D-72076 Tübingen, Germany
[16] Centre for Astrophysics, University of Hertfordshire, College Lane, Hatfield, AL10 9AB, UK
[17] Instituto de Astrofísica e Ciências do Espaço, Universidade do Porto, CAUP, Rua das Estrelas, 4150-762, Porto, Portugal
[18] School of Physics and Astronomy, University of Leeds, West Yorkshire, Leeds LS2 9JT, UK
[19] Max-Planck-Institut für Astrophysik, Karl-Schwarzschild-Str. 1, D-85741 Garching, Germany
[20] European Southern Observatory, Karl-Schwarzschild-Str. 2, D-85748 Garching bei München, Germany
[21] SRON Netherlands Institute for Space Research, Landleven 12, 9747 AD, Groningen, The Netherlands
[22] Indian Institute of Space science and Technology, Thiruvananthapuram 695 547, India
[23] Dublin Institute of Advanced Studies, Fitzwilliam Place 31, Dublin 2, Ireland
[24] SOFIA Science Center, Deutsches SOFIA Institut, NASA Ames Research Center, Moffett Field, CA, 94035, USA

ABSTRACT

Context. Circumstellar disks around massive stars could mediate the accretion onto the star from the infalling envelope, as well as minimise the effects of radiation pressure. Despite such a crucial role, only few convincing candidates have been provided for disks around deeply embedded O-type (proto)stars.

Aims. In order to establish whether disk-mediated accretion is the formation mechanism for the most massive stars, we have searched for circumstellar, rotating disks around a limited sample of 6 luminous ($>10^5 L_\odot$) young stellar objects. These have been selected in such a way as to maximize the likelihood of association with disk+jet systems, based on their IR and radio properties.

Methods. We used ALMA with ~0.′′2 resolution to observe a large number of molecular lines, typical of hot molecular cores. In this paper we limit our analysis to two disk tracers (methyl cyanide, CH_3CN, and its isotopologue $^{13}CH_3CN$), and an outflow tracer (silicon monoxide, SiO).

Results. We reveal many cores, although their number depends dramatically on the target. We focus on the cores that present prominent molecular line emission. In 6 of these a velocity gradient is seen across the core, with three cases showing evidence of Keplerian-like rotation. The SiO data reveal clear but poorly collimated bipolar outflow signatures towards two objects only. This can be explained if real jets are rare (perhaps short lived) in very massive objects and/or stellar multiplicity significantly affects the outflow structure. For all cores with velocity gradients, the velocity field is analysed through position–velocity plots to establish whether the gas is undergoing rotation with $v_{rot} \propto R^{-\alpha}$, as expected for Keplerian-like disks.

Conclusions. Our results suggest that in 3 objects we are observing rotation in circumstellar disks, with 3 more tentative cases, and 1 core where no evidence for rotation is found. In all cases but one, we find that the gas mass is less than the mass of any embedded O-type star, consistent with the (putative) disks undergoing Keplerian-like rotation. With the caveat of low-number statistics, we conclude that the disk detection rate could be sensitive to the evolutionary stage of the YSO. In young, deeply embedded sources, the evidence for disks could be weak because of confusion with the surrounding envelope, while in the most evolved sources the *molecular* component of the disk could have already been dispersed. Only in those objects that are at an intermediate stage of the evolution, the molecular disk would be sufficiently prominent and relatively less embedded to be detectable by mm/submm observations.

Key words. Stars: early-type – Stars: formation – ISM: molecules – Accretion, accretion disks

1. Introduction

How do massive stars form? A growing number of both observational and theoretical studies center on this topic. Recent years have seen significant progress (Tan et al. 2014) and we can now claim that numerical simulations adequately describe the formation of the most massive stars (Krumholz et al. 2007a; Kuiper et al. 2010; Peters et al. 2010). Observations are still lagging behind, but the dramatic improvement in sensitivity and/or resolution, offered by a number of facilities in recent years (*Herschel*, NOEMA, ALMA), is now allowing a quantum leap in our knowledge of the formation process of all stars, in general, and of early-type stars, in particular.

As in the low-mass case, disks around OB-type stars play an important role in angular momentum transfer (Rosen et al. 2012), but their existence is particularly crucial in allowing accretion to proceed, overcoming the powerful radiation pressure of luminous protostars (Krumholz et al. 2009; Kuiper et al. 2011; Peters et al. 2011; Klassen et al. 2016). In their comprehensive review, Beltrán & de Wit (2016) have summarized the current evidence for disks around intermediate- ($\sim$2–7 $M_\odot$) and high-mass ($\gtrsim$7 $M_\odot$) stars, from the embedded to the optically visible phase. Comparison between this recent review and the previous one by Cesaroni et al. (2007) shows that, while little doubt can now be cast about the existence of disks around B-type (proto)stars, those around O-type stars remain elusive. Observational evidence for massive cores, possibly undergoing (solid-body) rotation and containing newly born early-type stars has been provided by various authors (see e.g. Beltrán & de Wit 2016, Zapata et al. 2015). However, despite the prediction that Keplerian rotation could be seen up to 1000 AU radii (see Fig. 4 of Kuiper et al. 2011), only one convincing case is known of a Keplerian disk around a deeply embedded (proto)star exceeding the (approximate) threshold of $\sim$15 $M_\odot$ separating B- from O-type stars (Mottram et al. 2011b). This is AFGL 4176, for which Johnston et al. (2015) derive a stellar mass of 25 $M_\odot$ corresponding to an O7 spectral type. Not surprisingly, this result has been obtained thanks to the resolution *and* sensitivity of the Atacama Large Millimeter/submillimeter Array (ALMA).

In fact, prior to the finding of Johnston and collaborators, ALMA had already been crucial in placing the existence of disks around B-type stars on solid ground. While evidence for such disks was provided by various authors (see Cesaroni et al. 2007, Beltrán & de Wit 2016, and references therein), it was unclear whether disk-mediated accretion is the standard mechanism for the formation of B-type stars. With this in mind, we performed ALMA observations of two selected targets, with luminosities of $\sim$10^4 $L_\odot$ and associated with bipolar nebulae and hot molecular core (HMC) tracers. Our observations confirmed the presence of Keplerian disks, rotating about stellar masses of 9–18 $M_\odot$ (Sánchez-Monge et al. 2013, 2014; Beltrán et al. 2014), which indicates a continuity in the formation process from solar-type to B-type stars.

Based on this successful project, we have taken the study a step further and extended our disk search to the most massive stars. All models predict the existence of disks around such stars, although it is possible that their structure, size, and lifetime depend upon the formation process. Circumstellar disks are a natural outcome of the Bondi accretion process depicted by Keto (2002, 2003, 2007) and maintain their overall structure and velocity field even while partly ionized. The monolithic-accretion theory by McKee & Tan (2003) – in its modern incarnations by Krumholz et al. (2007b, 2009) – implies highly fragmented disks, encompassing binary and even multiple systems. More critical could be the situation of disks in the competitive accretion scenario by Bonnell et al. (2006), where a highly dynamical process favours the formation of the most massive stars in the gravitational well of a rich stellar cluster. Such a perturbed scenario could have even more dramatic consequences for the disk structure than just fragmentation: disks might be truncated or destroyed and reformed on relatively short (dynamical) timescales. In conclusion, the observable disk parameters are potentially useful to get an insight on the OB-type star formation process itself.

With all of the above in mind, we performed ALMA observations of a selected sample of luminous ($>$10^5 $L_\odot$) YSOs to investigate the presence of disks and possibly establish their characteristics. This article summarizes the preliminary findings of our study, while a detailed description of each source will be given in forthcoming dedicated papers. In the following, we explain how the targets were selected (Sect. 2), describe the observations and data reduction (Sect. 3), present the main results (Sect. 4), and analyse our findings to draw conclusions on the existence of disks around O-type (proto)stars (Sects. 5 and 6). Finally, a summary is given in Sect. 7.

2. Target selection and characterization

Our goal is to establish whether disk accretion is the common mechanism for the formation of O-type stars. We thus chose 6 targets from the "toroid" sample of Beltrán et al. (2005, 2011a) and the RMS survey database[1] (Lumsden et al. 2013; Urquhart et al. 2008), which satisfy most of the following criteria:

– luminosity $>$10^5 $L_\odot$, the minimum value for O-type stars;
– presence of a jet/outflow, from previous studies and/or data available to us, based on the assumption that disks are associated with bipolar flows ejected along the disk rotation axis;
– known association with a hot molecular core and/or mid-IR colours typical of young massive (proto)stars ($S_{21\mu m}/S_{8\mu m} \gtrsim 2$; Lumsden et al. 2013);
– distance below 8 kpc, to maximize the number of feasible targets without reducing the spatial resolution too much.

The 6 targets are given in Table 1 with their equatorial coordinates, LSR velocity ($V_{\rm LSR}$), bolometric luminosity ($L_{\rm bol}$), mass of the molecular clump[2] enshrouding the corresponding star forming region ($M_{\rm gas}$), and distance (*d*). The values of $L_{\rm bol}$ for G17.64, G345.49, and G345.50 have been taken

Send offprint requests to: R. Cesaroni, e-mail: cesa@arcetri.astro.it

---

[1] http://rms.leeds.ac.uk/cgi-bin/public/RMS_DATABASE.cgi
[2] We refer to "clumps" as pc-scale structures, as opposed to "cores", whose sizes are below $\sim$0.1 pc.

Table 1. Targets for the ALMA observations with their main parameters, obtained from the literature.

name	other names	α(J2000) (^{h} ^{m} ^{s})	δ(J2000) ($°$ $'$ $''$)	$V_{\rm LSR}$ (km s^{-1})	d (kpc)	$L_{\rm bol}$ ($10^5 L_\odot$)	$M_{\rm gas}{}^a$ ($10^3 M_\odot$)	Ref.^{c}
G17.64+0.16	AFGL 2136	18 22 26.370	−13 30 12.00	22.5	2.2	1.0	0.20	1
G24.78+0.08		18 36 12.661	−07 12 10.15	111.0	7.7	2.2	4.8	2, 3
G29.96−0.02	W43 S	18 46 03.665	−02 39 22.00	98.0	5.26	5.8	1.3	4, 5
G31.41+0.31		18 47 34.315	−01 12 45.90	96.5	7.9	2.6	5.2	3, 6
G345.49+1.47		16 59 41.610	−40 03 43.30	−12.6	2.4^b	1.5	1.2	1
G345.50+0.35		17 04 22.870	−40 44 23.50	−17.8	2.0	1.0	0.55	1

^{a} Computed from the flux density at 870 μm obtained from the ATLASGAL data, assuming a dust temperature of 50 K, a dust absorption coefficient $\kappa_{\rm dust} = 2$ cm^{2}g^{-1} (Ossenkopf & Henning 1994), and a gas-to-dust mass ratio of 100.
^{b} We prefer the spectrophotometric distance estimate by Moisés et al. (2011) to the kinematic distance of 1.6±0.1 kpc by Urquhart et al. (2008).
^{c} References for distance and luminosity: 1. RMS database; 2. Forster & Caswell (1989); 3. this paper; 4. Beltrán et al. (2013); 5. Zhang et al. (2014); 6. Cesaroni et al. (1994a)

from the RMS database[3]. For G29.96 we used the estimate of Beltrán et al. (2013), based on the Hi-GAL data, scaled to the new distance estimate of 5.26 kpc (Zhang et al. 2014). For G24.78 and G31.41, we have estimated $L_{\rm bol}$ by integrating under the spectral energy distribution reconstructed using the data from various surveys (Hi-GAL/*Herschel*, WISE, MSX, MIPSGAL/*Spitzer*). $M_{\rm gas}$ has been computed from the flux density at 870 μm obtained from the ATLASGAL[4] data (Schuller et al. 2009; Contreras et al. 2013), assuming an arbitrary dust temperature $T_{\rm dust} = 50$ K, a dust absorption coefficient $\kappa_{\rm dust} = 2$ cm^{2}g^{-1} at 870 μm (Ossenkopf & Henning 1994), and a gas-to-dust mass ratio of 100.

One sees that 3 sources lie at ∼2 kpc and the other 3 at ∼6–8 kpc. While this makes it difficult to compare the properties of the different objects, it allows us to investigate possible biases related to the distance.

We can get a hint on the evolutionary stage of the star forming region to which the targets belong, by inspecting the far-IR colour temperature, $T_{\rm c}[160 − 70]$, between 70 and 160 μm and the ratio $L_{\rm bol}/M_{\rm gas}$. The latter is believed to be a good proxy for the source age (see e.g. McKee & Tan 2003, Elia et al. 2010), as the gas mass is converted into stars during the process of star formation. The former is very sensitive to the temperature of the clump enshrouding the star forming region, as the typical spectral energy distribution of high-mass YSOs peaks around ∼100 μm (see e.g. van der Tak 2000, Cesaroni et al. 2015). Since the environment is progressively heated by the newly formed stars, one expects an increase of the dust temperature with time and thus an increase of $T_{\rm c}[160 − 70]$ with age. In Fig. 1, we plot these two parameters for our targets, for which we obtained the far-IR fluxes from the Hi-GAL data (Molinari et al. 2010, 2016). Indeed both parameters give consistent age indications: colder sources have lower $L_{\rm bol}/M_{\rm gas}$ ratios, and vice versa. On this basis, the targets can be grouped

into three pairs with progressively increasing age: G24.78 and G31.41; G345.49 and G345.50; and G17.64 and G29.96.

A word of caution is in order for the luminosity and mass estimates. The former assume isotropic emission, but inclination with respect to the line of sight could play a role if the clumps are not spherically symmetric and opacity is non negligible. For example, the flash-light effect can lead to underestimating the luminosity by an order of magnitude (see Zhang et al. 2013), if the bipolar structure is seen edge-on. Vice versa, a pole-on view may cause a significant overestimate of the luminosity. Our estimated luminosity may also be affected by the radiation from nearby more evolved massive stars, which are only loosely connected with the target of interest. An illuminating example is that of G29.96. Although de Buizer (2002) has demonstrated that the HMC is a prominent mid-IR emitter, the nearby ultracompact Hɪɪ region is known to be associated with an O5–O6 star (Martín-Hernández et al. 2003), which may therefore contribute to a significant fraction of $L_{\rm bol}$ (up to 92%; see Vacca et al. 1996). The value of $5.8 \times 10^5 L_\odot$ is thus an upper limit to the luminosity of the HMC. While a similar conclusion may hold also for the other five cores, the contribution from nearby stars is rather uncertain in these cases, as such stars have not been directly observed.

Finally, we note that a priori the mass estimate can be affected by significant errors (a factor of ∼2; see Maud et al. 2015a), mostly due to the uncertainties on $\kappa_{\rm dust}$ and $T_{\rm dust}$. However, the latter is unlikely to vary more than $T_{\rm c}[160 − 70]$, namely ∼40%, while the former should not change much from source to source, because the selected sample is relatively homogeneous. Assuming that $\kappa_{\rm dust}$ is indeed the same in all sources, the points in Fig. 1 can only shift systematically along the y-axis, thus preserving the observed trend.

3. Observations and data analysis

ALMA was employed to perform observations towards the positions given in Table 1. The number of 12-m antennas used ranged from 38 to 41. The correlator was set in such a way as to cover a large number of lines, with special attention to the CH$_3$CN(12–11), ^{13}CH$_3$CN(13–12), and SiO(5–4) rotational transitions. A broad 1.8 GHz spectral unit was also used to obtain a sensitive continuum measurement at ∼218 GHz.

---

[3] The RMS luminosities have been derived from the method described in Mottram et al. (2011a), updated with the Hi-GAL/*Herschel* far-IR fluxes (Molinari et al. 2010, 2016), where available (Mottram et al. in prep.).
[4] The ATLASGAL project is a collaboration between the Max-Planck-Gesellschaft, the European Southern Observatory (ESO), and the Universidad de Chile.
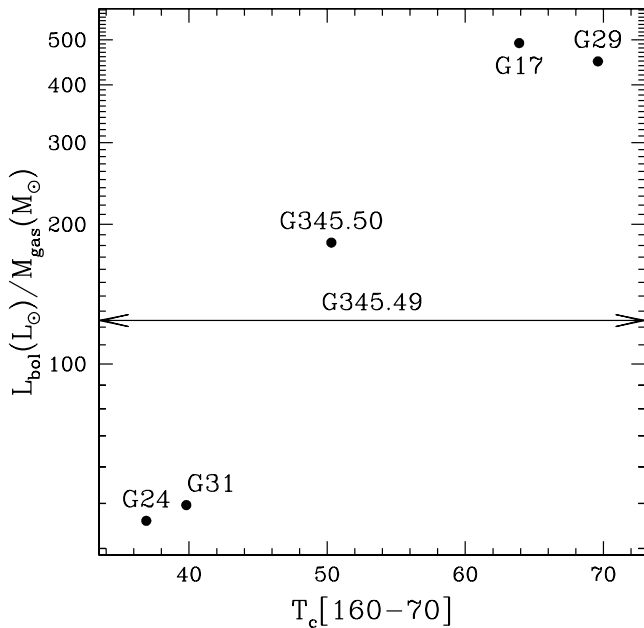
Fig. 1. Plot of the ratio between the bolometric luminosity and the mass of the associated molecular clump versus the colour temperature obtained from the ratio between the far-IR flux densities at 70 and 160 μm, for all the sources of our sample. The horizontal line denotes that for source G345.49 no estimate of $T_c[160-70]$ is possible, because the source lies beyond the region covered by the Hi-GAL survey.

Table 2. Spectral windows covered by the correlator setup, with corresponding spectral resolutions and noise per channel.

frequency range (GHz)	resolution (kHz)	1σ noise[a] (mJy/beam)	molecule[b]
216.976–218.849	1953.1	1.3	SiO
219.533–219.767	488.3	1.5	
220.303–220.537	244.1	2.0	CH_3CN
220.533–220.767	244.1	1.9	CH_3CN
221.213–221.447	488.3	1.8	$CH_3CN\ v_8=1$
231.803–232.037	488.3	1.8	$^{13}CH_3CN$
232.033–232.267	488.3	1.6	$^{13}CH_3CN$
232.903–233.137	488.2	1.7	
233.133–233.367	488.3	1.5	
235.283–235.517	488.3	1.4	
235.853–236.087	488.3	1.6	
236.083–236.317	488.3	1.5	
236.313–236.547	488.3	1.6	

[a] The noise has been estimated in the channel corresponding to the strongest emission in the bandwidth. Note that this value is only indicative, as it can change significantly from source to source.
[b] Only the species analysed in the present study are reported.

The primary beam of the 12 m antennas at this frequency is ~26″. The frequency range of each spectral unit and the corresponding spectral resolution and sensitivity are given in Table 2, where we also indicate which spectral units cover the species discussed in the present article. Note that the frequency coverage is not exactly the same for all sources, because pairs of targets were observed in track sharing mode, which requires a compromise for the LSR velocity.

The observations were conducted during Cycle 2 in July and September 2015, with the array in an extended configuration with baselines ranging from 40 m to 1500 m. Flux calibration was obtained through observations of the planetary system bodies Titan and Ceres. The phases were calibrated from interleaved observations of the quasars J1733–1304 (for G17.64 and G24.78), J1851+0035 (for G29.96 and G31.41) and J1709–3525 (for G345.49 and G345.50). The gain calibrators, separated from the sources on the sky by 2°–5°, were observed every 6 min. The bandpass correction was obtained by observing the bright quasars J1733–1304, J1617–5848 (in July) and J1924–2914 (in July and September). The on-source observing time per source was about 50 min.

The calibration and imaging were carried out in CASA. Imaging was performed on each spectral window using the CLEAN task, with the robust parameter of Briggs (1995) set to 0.5, as a compromise between resolution and sensitivity to extended emission. The resulting images have a synthesized CLEANed beam of about 0″.2. The rms noise level in a spectral channel is given in Table 2, while in the continuum maps the noise ranges from 0.2 to 1 mJy/beam and is mostly limited by the dynamic range.

3.1. Continuum image and continuum subtraction

The usual method to create an image of the continuum emission and subtract it from the data, consists in identifying the channels where no line emission is present, under the assumption that these channels correspond to the continuum level. Subtraction can then be performed in the uv or image plane. While this method can be easily adopted for sources with a relatively low level of line emission, in our case almost all the observed spectra present a "line forest", which makes the visual identification of a continuum level extremely difficult.

We thus decided to employ a statistical method which estimates the continuum level at each position of the map from the distribution of the intensity in the different channels of the spectrum at that position. This is done within the python-based tool STATCONT (Sánchez-Monge et al. 2017), which is freely accessible[5]. In practice, we compute the median, μ, and standard deviation, σ of this distribution, and assume that the continuum level is equal to $\mu - \sigma + \sigma_0$, where σ_0 is the mean value of the noise over a region void of emission. This latter correction is needed because the expression $\mu - \sigma$ would result in a negative value in those positions where no emission is detected, and in all cases it would underestimate the correct continuum emission. In this process, the strongest channels are progressively excluded through an iterative procedure ("sigma clipping"), where all channels whose flux lies beyond the interval $\mu \pm 2\sigma$ are not used in the next step of the calculation of μ and σ. The loop stops when the values of μ and σ do not change anymore. The continuum image obtained in this way is then subtracted from the corresponding data cube.

The validity of our procedure is described in detail and tested with numerical simulations in Sánchez-Monge et al. (2017). Note that the method is applied to each spectral win-

---

[5] http://www.astro.uni-koeln.de/šanchez/statcont

dow of the correlator, independently of the others. This makes it acceptable to neglect the dependence of the continuum emission on frequency, since the bandwidths are relatively narrow (<2 GHz).

4. Results

In this section, we present and discuss the main findings of our observations, focusing on the comparison between the different sources. A more detailed analysis of each target will be performed in a number of dedicated papers.

4.1. Continuum emission

The maps of the continuum emission of the 6 targets are shown in Fig. 2. All of these have been obtained from the spectral unit with the largest bandwidth (1.8 GHz), using the procedure described in Sect. 3.1. One sees that most maps present a clumpy structure, with the emission being concentrated in a single source only in two cases (G17.64 and G31.41). In particular, in G17.64 the continuum source is basically unresolved with a synthesised beam of $\sim$0.″15, and the emission could entirely be due to free-free emission, based on the results of Menten & van der Tak (2004). The arc-like feature in G29.96 traces the rim of the cometary ultracompact (UC) H<small>II</small> region and is (at least partly) due to free-free continuum emission from the ionized gas. Prominent free-free emission is also contaminating one source in G24.78 (see Beltrán et al. 2007) and one in G345.49 (Guzmán et al. 2010), known from previous observations at centimeter wavelengths. All these three continuum sources (G29.96, G24.78, G345.49) are also clearly detected in the H30α recombination line, which is covered by our frequency setup.

All the other features detected above a 5σ level in Fig. 2 are dominated by dust emission and trace compact molecular cores. It thus appears that the level of fragmentation in the observed regions varies quite a lot, from compact objects such as G17.64 and G31.41 (although on different spatial scales), to very clumpy regions like G24.78 and G345.49, where visual inspection identifies up to 9 fragments in each of them. In G31.41, a large continuum opacity could justify the (apparent) homogeneity of the core, but even so, the putative fragments would be "squeezed" inside a more compact region than in the other targets. The variety of clumpiness is better illustrated by Fig. 3, where the same data as in Fig. 2 are shown with constant physical scales. The most distant fields such as G31.41 might indeed contain more undetected cores, but the different morphologies observed in the various sources cannot be explained by the different spatial resolutions alone. This is further emphasised in Fig. 4, where the fraction of the continuum flux density recovered by the interferometer is plotted as a function of the source distance. For this purpose we have divided the integrated flux density over the whole ALMA map by the flux density measured inside a 33″ beam (similar to the ALMA primary beam) towards the phase center in the corresponding BOLOCAM GPS image (Ginsburg et al. 2013). Note that for the two sources not covered in the BOLOCAM survey (G345.49 and G345.50) we used the flux density mea-

sured by Faúndez et al. (2004) at 1.2 mm. For consistency with the BOLOCAM measurements, the fluxes were rescaled to a HPBW of 33″ by assuming a Gaussian source with the full width at half maximum measured by Faúndez and collaborators.

While on average the fraction of recovered flux in the ALMA data increases with distance to the source, a large spread is present at all distances. For example, both G24.78 and G31.41 are located at ~8 kpc, but an order of magnitude less flux is recovered for the former region compared to the latter. This indicates that variations in the level of clumpiness are real and not (entirely) due to different distances and mass sensitivities.

In conclusion, despite the similar luminosities, our targets are quite heterogeneous both in terms of evolutionary stage (see Sect. 2) and level of fragmentation.
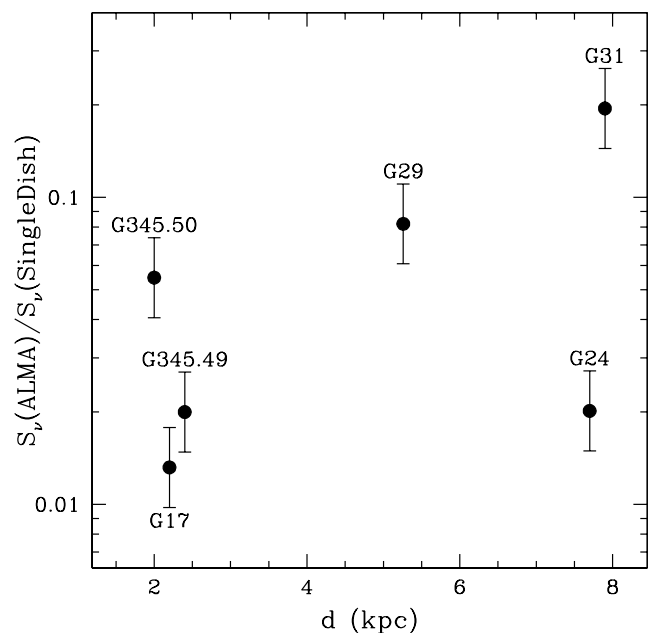

Fig. 4. Ratio between the total continuum flux density recovered by ALMA and that measured in a 33″ beam towards the phase center of each target (obtained from the BOLOCAM GPS images at 1.1 mm) versus source distance. The error bars correspond to 30% calibration uncertainty on the flux ratio.

4.2. Line emission

In Fig. 5 we show a template spectrum obtained by integrating the line emission from the HMC in G29.96, inside the contour corresponding to the 5σ level of the continuum map in Fig. 2. This spectrum clearly illustrates the plethora of lines covered by our setup.

The line identification process is a difficult and time-consuming task that goes beyond the scope of the present paper and will be performed in forthcoming articles. Here, we make only a qualitative comparison among the different targets in terms of line richness and intensity. For this purpose, we define two parameters: f, the fraction of spectral channels where line
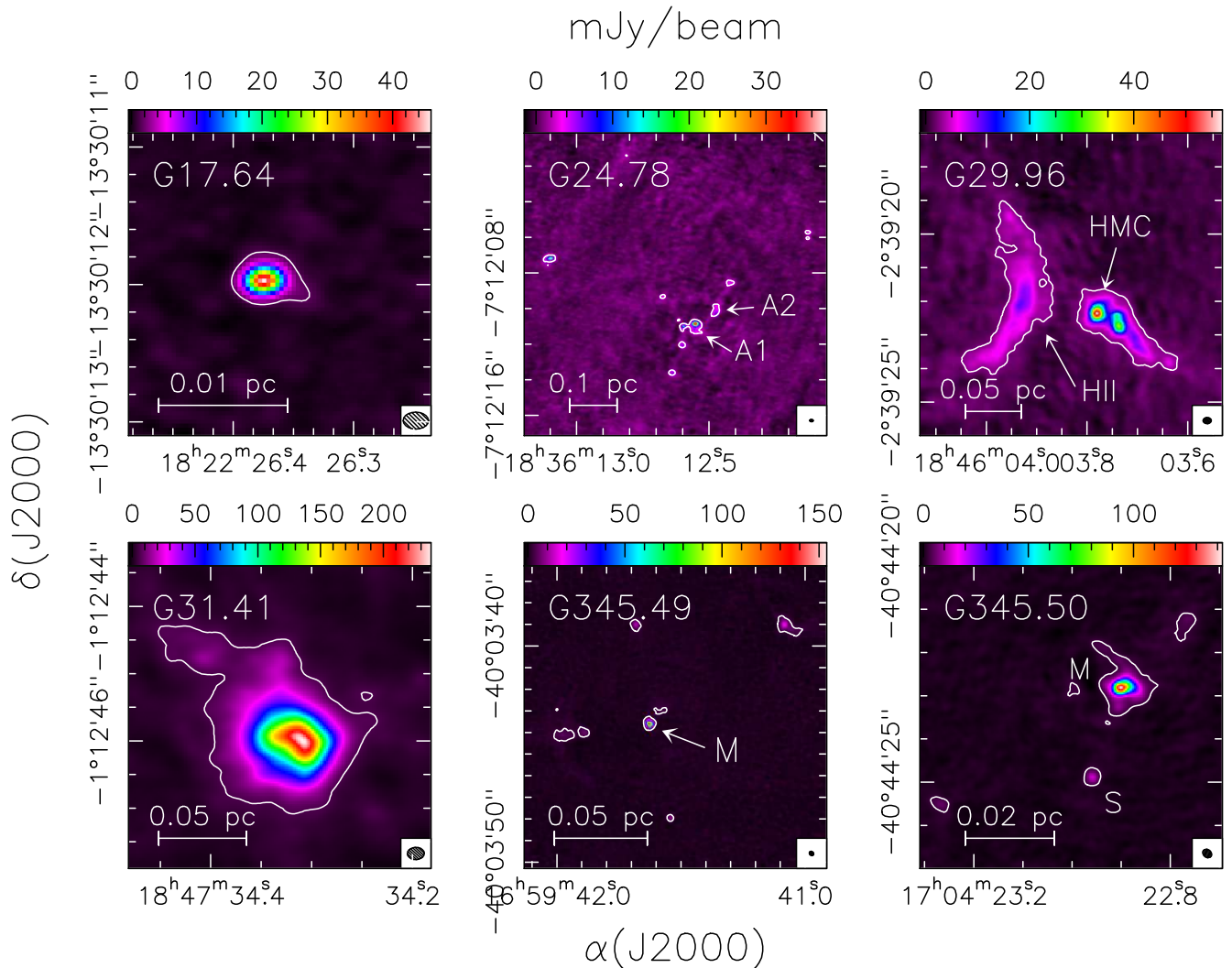
Fig. 2. Maps of the continuum emission at 218 GHz from the 6 targets observed. The solid contours correspond to the 5σ levels. The ellipse in the bottom right of each panel denotes the half-power width of the synthesised beam. The maps cover the whole region where emission is detected. The labels indicate the UC H II region in G29.96 and the cores that we will refer to in the present study. Note that the maximum recoverable scale in these images is $\sim 4''$, much greater than the diameter of the largest cores detected.

emission is detected, and I, the mean intensity per unit bandwidth of the emission in these channels, scaled by d^2 to take into account the different distances to the sources. We compute f and I for the largest bandwidth (~ 1.8 GHz) covered in our correlator setup. In practice, we consider the spectrum towards the peak of the continuum emission. When multiple continuum sources are detected, we select the strongest of them.

Table 3 gives the values obtained for our 6 targets. The obvious conclusion is that most of the cores are line rich, with the exception of G345.49. Also G17.64 seems line poor, but the low value of f is partly due to the fact that it is emission weak. In fact, although its mean intensity is half that of G345.49, the value of f is larger. Moreover, f in G17.64 is only 1.5 times lower than in G24.78, whose I is 19 times stronger. All this suggests that G17.64 is intrinsically more chemically rich than it appears. We will come back to this point in Sect. 5.1.

In the following, we will concentrate on a few molecular species: CH_3CN and its isotopologues, and SiO. This choice is dictated by the goal of our study, namely to search for cir-

Table 3. Richness (f) and mean intensity (I) of the line emission in the observed objects.

Name	f	I
	(%)	(mJy beam^{-1} kpc^2)
G17.64+0.16	23	0.12
G24.78+0.08	35	2.31
G29.96−0.02	79	1.32
G31.41+0.31	74	2.26
G345.49+1.47	17	0.25
G345.50+0.35	77	0.18

cumstellar disks and the associated bipolar jets/outflows. It is well known that methyl cyanide is an excellent hot core tracer and has proved successful in tracing the dense, hot gas in circumstellar disks around B-type (proto)stars (see e.g. Cesaroni et al. 2014, Sánchez-Monge et al. 2013). Since O-type stars are likely to be enshrouded by even larger and more massive envelopes than B-type stars, we also analyse the isotopologue
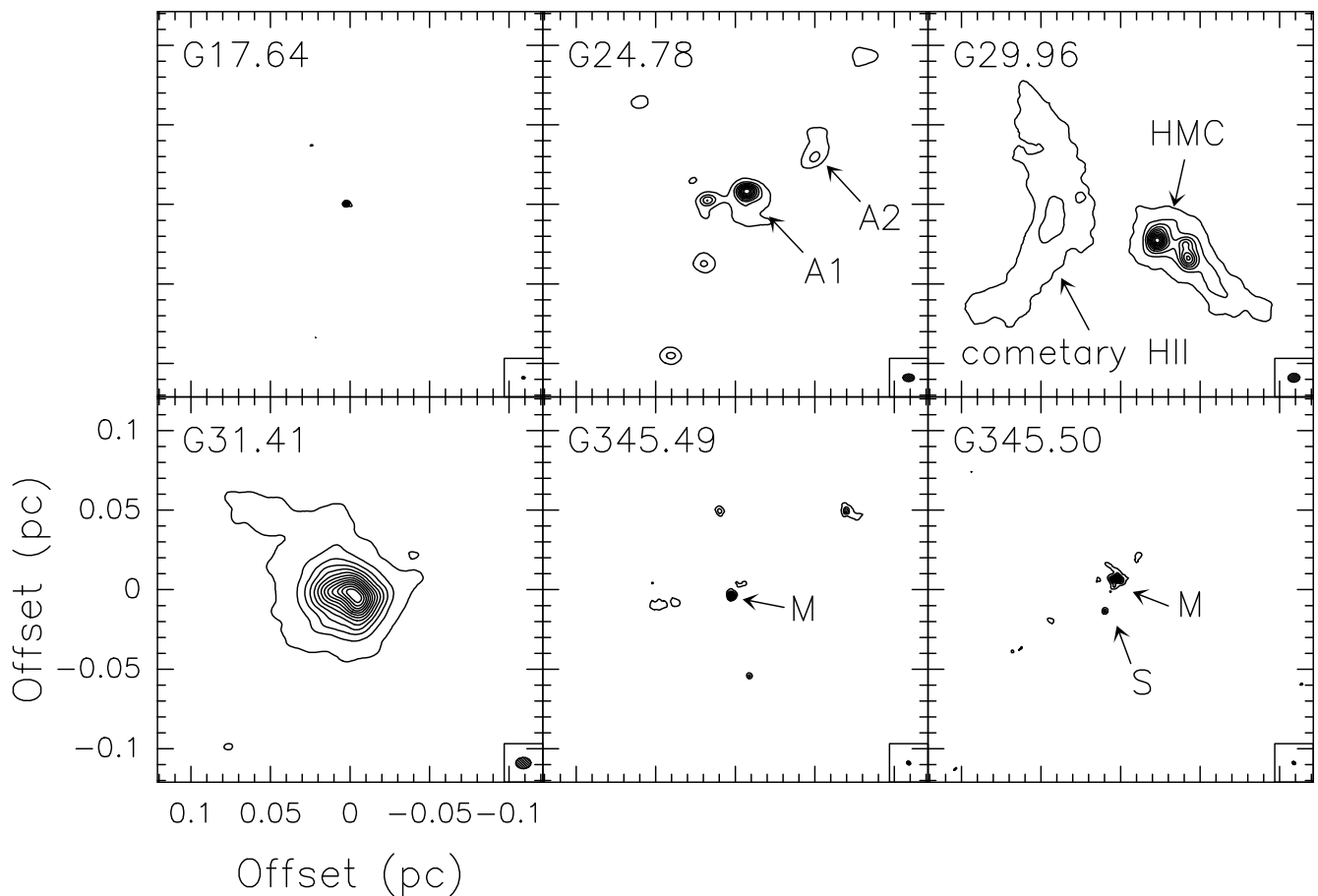
Fig. 3. Same as Fig. 2, with axes expressed in linear scale instead of angular scale. In order to facilitate the visual comparison between the different fields, the size of the region shown is the same for all maps. Symbols have the same meaning as in Fig. 2. The minimum, maximum, and step of the contour levels are: 1.5, 43.5, 3 mJy/beam for G17.64; 2.5, 52.5, 5 mJy/beam for G24.78; 2.5, 52.5, 5 mJy/beam for G29.96; 6, 222, 18 mJy/beam for G31.41; 2.5, 152.5, 5 mJy/beam for G345.49; 2.2, 138.6, 4.4 mJy/beam for G345.50. Note that the area shown in the maps lies inside the primary beam, whose half-power width is in all cases >0.25 pc.

$^{13}CH_3CN$, whose transitions are optically thinner and thus better suited to investigate the densest gas close to the star(s). As for the jets/outflows, the interaction between the outflowing gas and the surrounding environment is expected to cause shocks (see e.g. Kuiper et al. 2016), triggering the formation of silicon monoxide, which is indeed often observed in knots along the jet/outflow axis (see e.g. Bachiller et al. 1997, Gueth et al. 1998, Sollins et al. 2004, Cesaroni et al. 2005).

In order to get an idea at first glance of the morphology and kinematics of the dense gas in the circumstellar environment of our sources, in the top panels of Figs. 6 to 11 we show the map of the average emission over the $K=2$ component of $CH_3CN(12-11)$ at 220730.266 MHz and the corresponding 1st- and 2nd-moment maps, for each target. The same maps for the $^{13}CH_3CN(13-12)$ $K=2$ line at 232216.438 MHz are shown in the bottom panels of the same figures, for all sources except G17.64, where no $^{13}CH_3CN$ transition was detected. For the sake of comparison, we also plot two contours, corresponding to the 5σ level and the full width at half maximum (FWHM) of the 1.4 mm continuum emission. We have chosen the $K=2$ line because it provides us with the highest S/N and minimum contamination by other lines. The $K=0$ and 1 components would

be better in terms of S/N, but heavily overlap each other, which makes them unusable for kinematical studies.

The structure of the methyl cyanide emission varies significantly from source to source, but in all cases, except perhaps G17.64, clear velocity shifts of several km s^{-1} are detected in at least one of the cores traced by the continuum emission. These are seen also in the $^{13}CH_3CN$ maps. While the interpretation of these gradients is not trivial and will be discussed in Sect. 5, here we note that their mere existence indicates that the densest gas is not undergoing randomly oriented motions but has a well organized velocity field.

In a disk+jet system the SiO line should be emitted along the jet axis, namely perpendicular to the CH_3CN velocity gradient, which is tracing the disk. It is hence interesting to compare the maps of the two species. Unfortunately, the SiO emission could be properly imaged in only 4 sources (G17.64, G29.96, G31.41, and G345.50). In the other 2 targets (G24.78 and G345.49) the emission is resolved out by the interferometer, which is not sensitive to structures above a few arcsec. However, previous SMA observations of the SiO(5–4) line towards G24.78 (Codella et al. 2013), with better sensitivity to extended emission, have revealed a clear bipolar outflow, whose axis is indicated by the dashed line in the middle panel
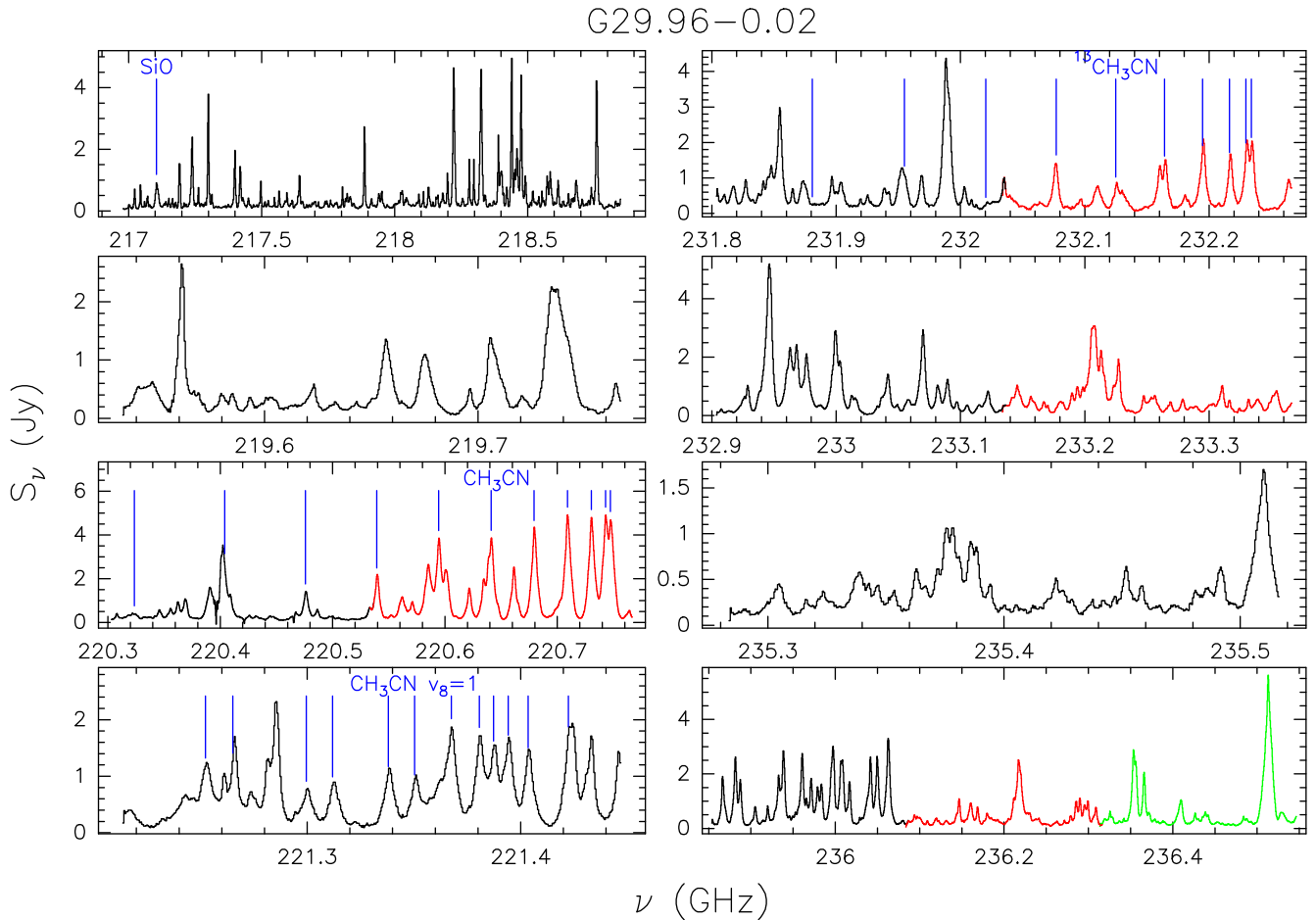
Fig. 5. Spectra obtained by integrating the emission over the 5σ contour level of the continuum map of the G29.96 HMC. The whole frequency range covered by our correlator setup is shown. Different colours in the same box correspond to different spectral windows of the correlator. The vertical lines mark the positions of the SiO(5–4), CH_3CN(12–11) ground state, CH_3CN(12–11) v_8=1, and $^{13}CH_3CN$(13–12) lines. Note that not all of these are detected and some of them are heavily blended with other transitions.
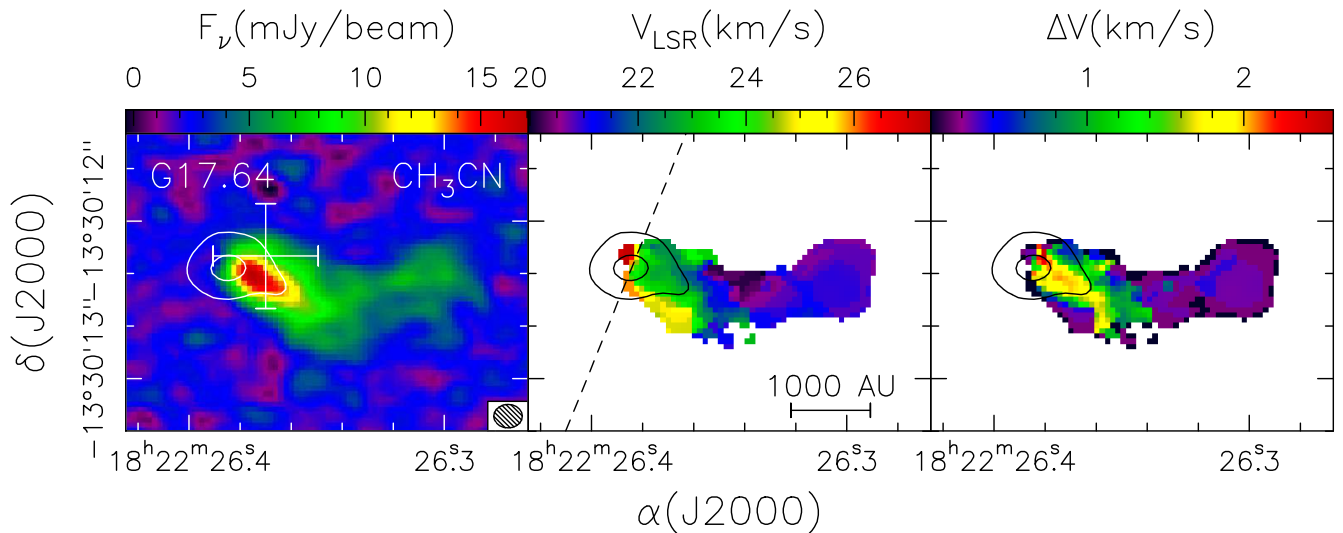
Fig. 6. Left. Map of G17.64 obtained by averaging the emission over the CH_3CN(12–11) K=2 line. The contours correspond to the 5σ (outer contour) and 50% level (inner contour) of the continuum emission. The cross marks the position, with errors, of the centimeter continuum source detected by Menten & van der Tak (2004). The synthesised beam is shown in the bottom right. **Middle.** Same as left panel, for the 1st-moment map. The dashed line indicates the direction of the axis of the ^{12}CO outflow detected by Kastner et al. (1994). **Right.** Same as left panel, for the 2nd-moment map.
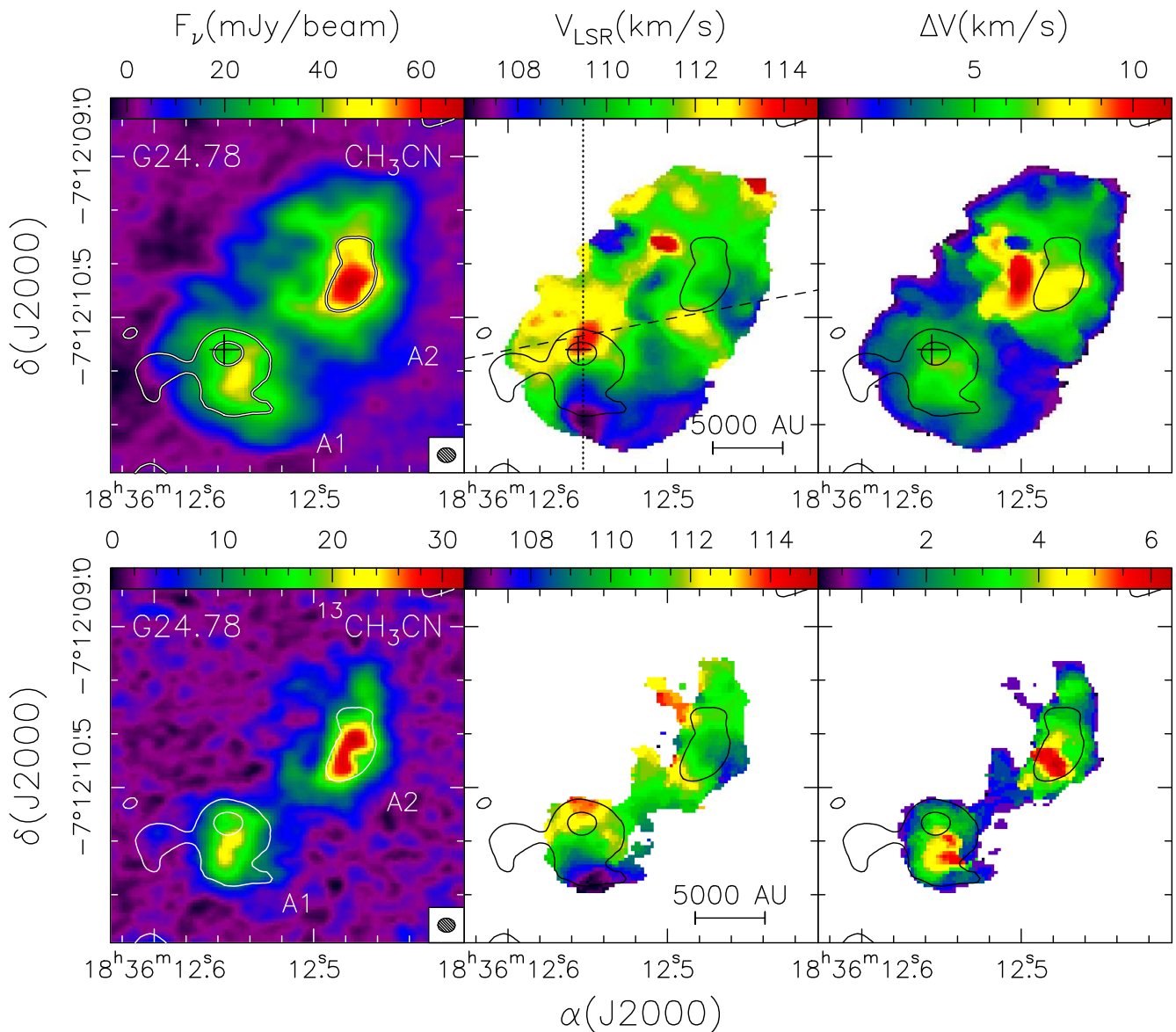
Fig. 7. Top. Same as Fig. 6, for G24.78. The cross in the top panels marks the position of the hypercompact Hɪɪ region studied by Beltrán et al. (2007) and the dashed line denotes the axis of the bipolar outflow detected by Codella et al. (2013) in the SiO(5–4) line. The dotted line indicates the direction adopted for the corresponding position–velocity plots. Labels A1 and A2 mark the corresponding HMCs, as in Fig. 2. **Bottom.** Same as top panels, for the $^{13}CH_3CN(13–12)$ K=2 line.

of Fig. 7. Furthermore, in G345.49, Guzmán et al. (2011) have mapped two large-scale bipolar outflows, one of which is associated with a radio jet centered on the main core detected by us, G345.49 M (see Sect. 5.5 and Fig. 2).

As for the 4 sources detected by us, in G17.64 the SiO emission looks compact and coincides with the continuum core (see Fig. 12), whereas a clear bipolar symmetry is present in G29.96, G31.41, and G345.50 (see Figs. 13–15), although the orientation with respect to the CH_3CN velocity gradient varies from source to source. Only in G29.96 are the two perpendicular, whereas in G31.41 the SiO axis is inclined by ~30° with respect to the prominent CH_3CN velocity gradient, and in G345.50 the situation appears much more complicated.

Note that the SiO emission does not appear to trace jet-like morphologies. On the contrary, cases like those of G29.96 suggest wide-angle winds. One may speculate that these are caused by interactions with companions inducing, e.g., precession of the outflow. This fact could be taken as indirect evidence for the presence of multiple sources inside the cores. Indeed, Peters et al. 2014) have demonstrated that wide-angle winds are created naturally when several stars form in the same gravitationally unstable accretion flow. Alternatively, these sources may not currently be driving jets (which could be rare and/or short lived in these massive YSOs), and the SiO may be tracing shocks between the wind and the surrounding outflow cavity wall.

5. Analysis: Searching for disks

Based on the results illustrated above, one may conclude that despite our attempt to select a homogeneous sample of O-type YSOs, the observed sources present significant differences
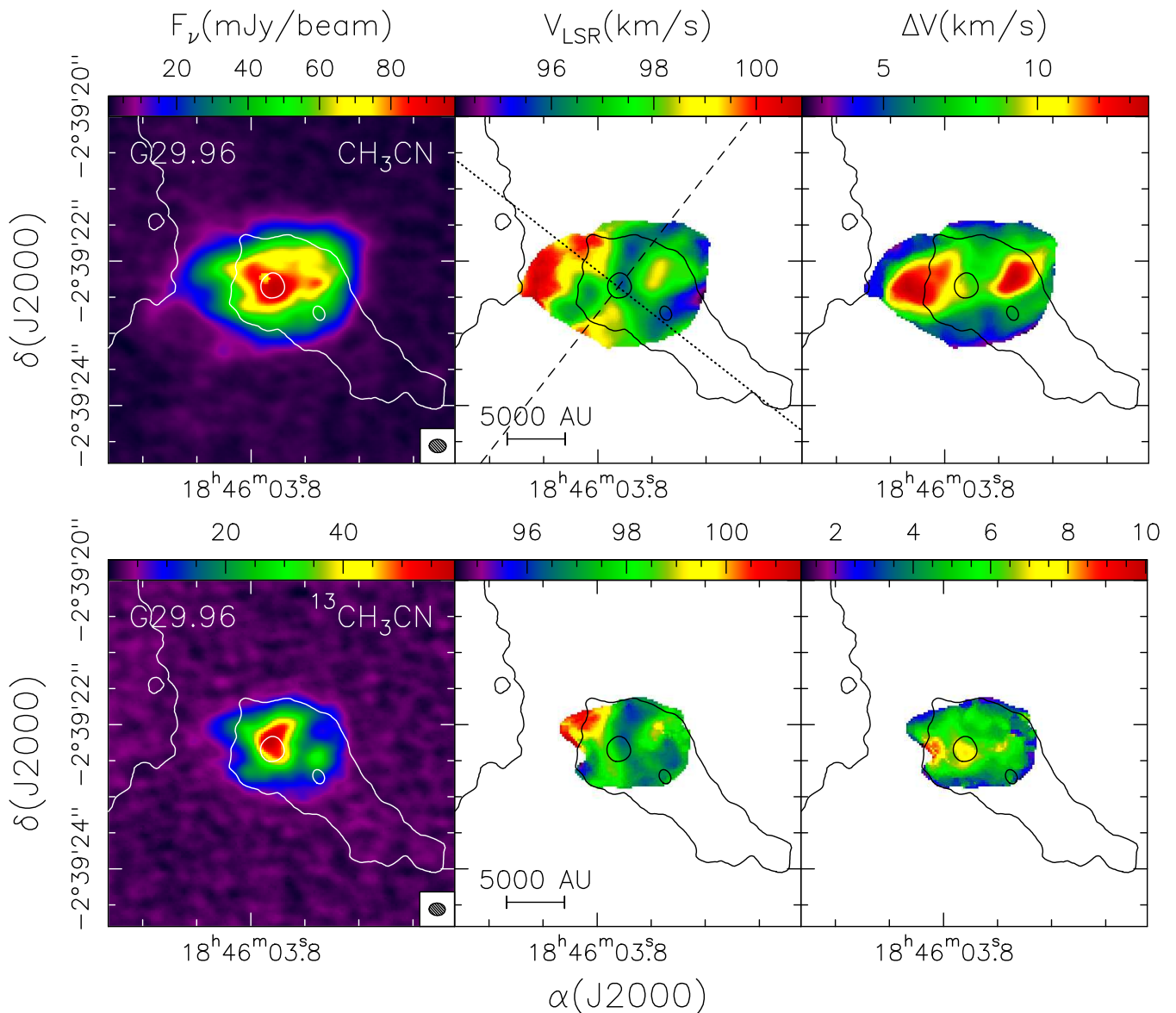
Fig. 8. Same as Fig. 7, for G29.96. The dashed line marks the direction of the bipolar outflow detected in the present study (see Fig. 13). The dotted line denotes the cut adopted for the PV plot in Fig. 17.

even among objects located at similar distances. Such heterogeneity mirrors the complexity of high-mass star forming regions, whose characteristics must depend not only on the properties of the large-scale environment but also on the evolutionary phase. The structure and even the mere existence of circumstellar disks may be very sensitive to these environmental factors. In the following, we study the dusty cores detected in our targets and investigate the possibility that some of these contain disks around massive stars.

In order to identify a rotating circumstellar disk from the data available to us, one may use two simple criteria: (i) the velocity gradient observed in CH_3CN should be roughly perpendicular to the associated SiO jet/outflow axis; (ii) the velocity should increase with decreasing distance to the star. The latter is based on the fact that the gas in accretion disks must fall onto the star conserving the angular momentum or settling in a Keplerian disk. While angular momentum transfer and the

presence of turbulence can affect this scenario, it seems reasonable to expect rotation to be faster towards the center, namely that rotation velocity scales with the distance R from the star as $v_{\rm rot} \propto R^{-\alpha}$, with $\alpha > 0$ ($\alpha=1/2$ corresponds to Keplerian rotation). In the following, we will refer to this as "Keplerian-like rotation".

Of course the scenario may be more complicated depending on the gas mass distribution inside R, the level of turbulence, the development of instabilities in the disk, and the effect of the magnetic field which could brake the rotation. Therefore, in extreme cases there could be no Keplerian-like motion even at very small radii, where the gravitational field is dominated by the star (see Peters et al. 2011). Despite all these caveats, should we find evidence for $v_{\rm rot} \propto R^{-\alpha}$, this would hint at the presence of Keplerian-like rotation and thus of a circumstellar disk. This type of rotation curve is recognizable in a position–
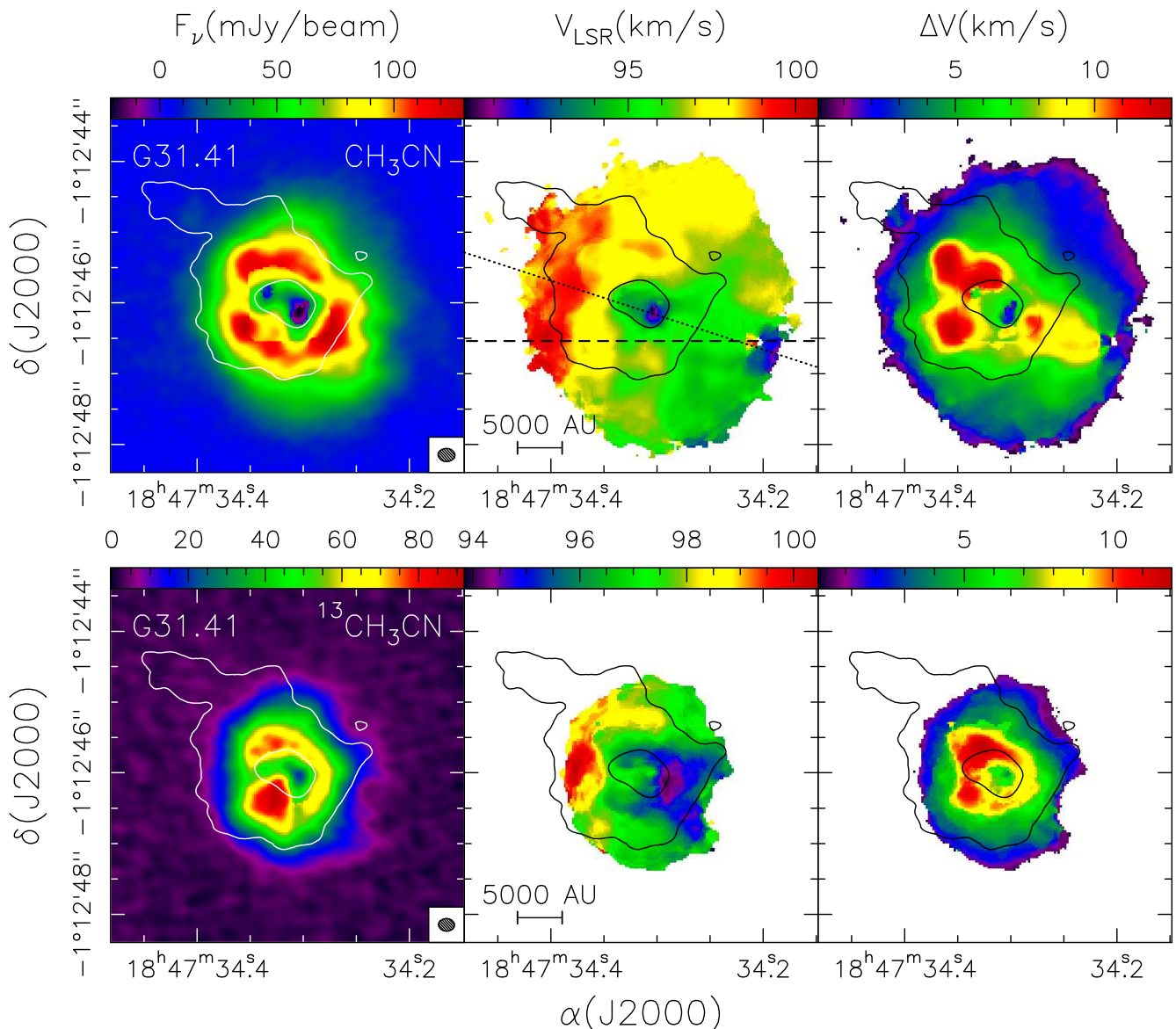
Fig. 9. Same as Fig. 7, for G31.41. The dashed line marks the axis of the bipolar outflow detected in the present study (see Fig. 14). The dotted line denotes the cut adopted for the PV plots in Fig. 19.

velocity (PV) plot because the emission outlines a "butterfly-shaped" pattern (see e.g. Cesaroni et al. 2005, 2014).

With this in mind, we analyse the most prominent velocity gradients observed in our sources. The purpose of Sects. 5.1 to 5.6 is to briefly outline the main characteristics of each source with special attention to the velocity field of the gas, which is the best suited tool to unveil the presence of rotation around the embedded star(s). Such a source-by-source description is necessary because of the significant differences among the targets. The results obtained from this analysis will be then summarized and put into context in Sect. 6.

5.1. G17.64

In G17.64, also known as AFGL 2136, the continuum source presents only marginal emission of hot-core tracers such as CH_3CN and the SiO emission does not appear to be tracing a bipolar flow, as noted in Sect. 4.2. The elongated and bent shape of the CH_3CN map (see Fig. 6) rather suggests that this molecule might be partially tracing the border of the red-shifted lobe of the bipolar outflow, oriented approximately SE–NW, imaged by Kastner et al. (1994) and Maud et al. (2015b). However, this interpretation is inconsistent with the velocity of most CH_3CN emission, which appears blue-shifted, whereas the outflow lobe to the NW is red-shifted. An alternative possibility – purely speculative at present – is that the CH_3CN emission might be tracing infall towards the continuum source. In this scenario, the gas would flow from west to east in the plane of the sky moving towards the observer, thus explaining the blue-shifted emission in Fig. 6. Once the gas has reached the continuum source, it would spiral down onto it making a 180° turn, which could justify the red-shifted emission at the continuum peak.
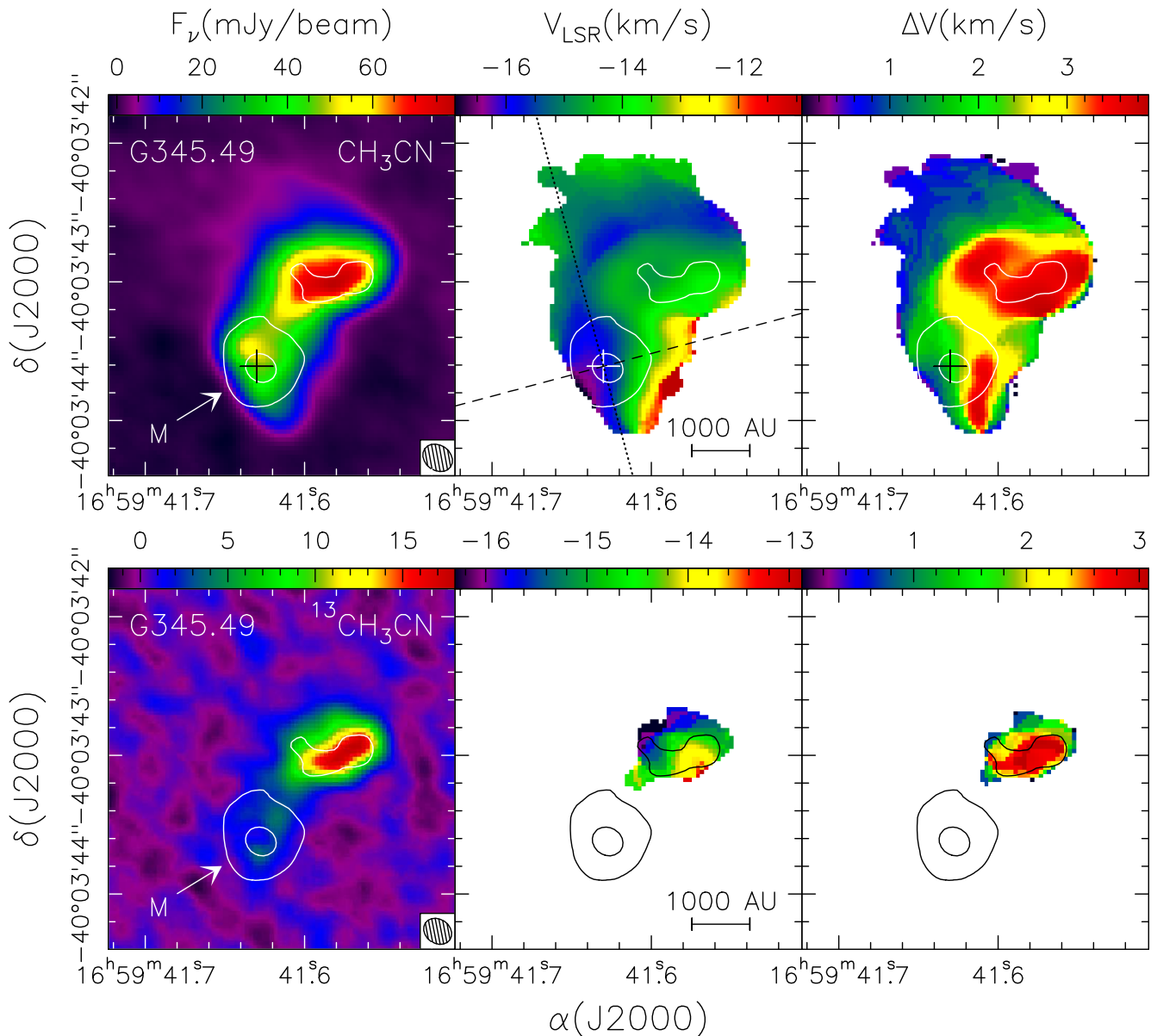
Fig. 10. Same as Fig. 7, for G345.49. The cross marks the position of the central knot of the radio jet imaged by Guzmán et al. (2010), while the dashed line denotes the radio jet axis. Label M marks the core of interest for our study, as in Fig. 2.

In any case, we conclude that no evidence for a circumstellar disk can be obtained from the molecular line emission in this object. Since the source appears to be the most evolved of our sample (see Fig. 1), one could speculate that the molecular component of the disk has been substantially dispersed. This hypothesis seems supported by the result discussed in Sect. 4.2, namely that G17.64 is emission weak but chemically rich. Such a chemical complexity is consistent with the (former) presence of a HMC, while the faint line emission indicates that only a remnant of the pristine dense molecular gas is left.

If G17.64 is the most evolved of our sources, one expects to find an HII region associated with it. No radio continuum has been detected at 6 cm with the VLA at ~2″ resolution (Urquhart et al. 2009; see also the on-line RMS database), which would hint at a young source. However, Menten & van der Tak (2004) have revealed a bright (>2000 K

at 43 GHz) free-free continuum source, whose position is consistent, within the uncertainties, with the continuum peak seen with ALMA (see Fig. 6). Furthermore, inspection of the corresponding NVSS (Condon et al. 1998) field reveals a peak of continuum emission at 20 cm of ~3 mJy/beam. These findings suggest that G17.64 could be related to an HII region, although considering the large NVSS image resolution (45″), an association remains ambiguous.

5.2. G24.78

Various studies (Beltrán et al. 2004, 2005, 2011b) have provided evidence for the existence of up to three rotating cores in the region observed with ALMA. Here, we focus on the most prominent core (A1, following the notation by Beltrán et al. 2005) containing the hypercompact HII region studied by
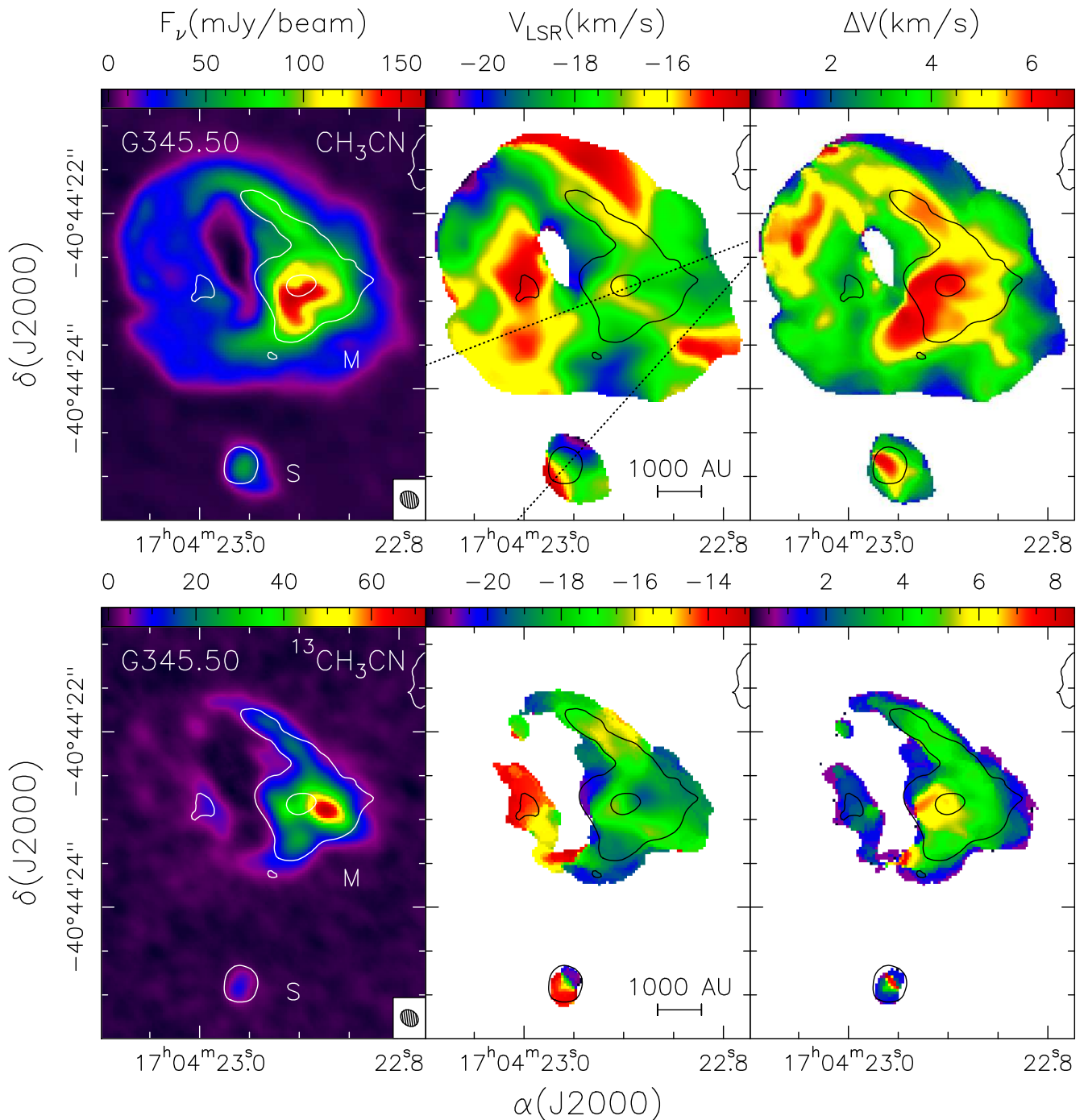
Fig. 11. Same as Fig. 7, for G345.50. Labels M and S mark the corresponding cores, as in Fig. 2. The dotted lines denote the cuts adopted for the PV plots in Figs. 22 and 23.

Beltrán et al. (2007) and indicated by a cross in Fig. 7. From this figure one clearly sees that the gas velocity in the core is red-shifted to the north and blue-shifted to the south, a result which looks different from the NE–SW velocity gradient found by Beltrán et al. (2004, 2005, 2011b). Such a difference is likely due to the different uv coverages of the various data sets. Given the superior image fidelity of ALMA on scales ≲1″, we believe that our data provide a better representation of the gas structure and motion, than those obtained with other (sub)mm interferometers. Note also that the N–S velocity gradient detected by

us (~240 km s^{-1} pc^{-1}) appears perpendicular to the SiO flow imaged by Codella et al. (2013), whose axis is represented by the dashed line in Fig. 7.

While all the above is suggestive of rotation of core A1 about the outflow axis, a couple of caveats are in order.

First of all, according to Codella et al. (2013) and Vig et al. (2008) the outflow is not associated with A1, but the powering source should either coincide with A2 (the other core to the NW, where we do not detect a velocity gradient) or lie between A1 and A2. While this is certainly possible, the geometrical
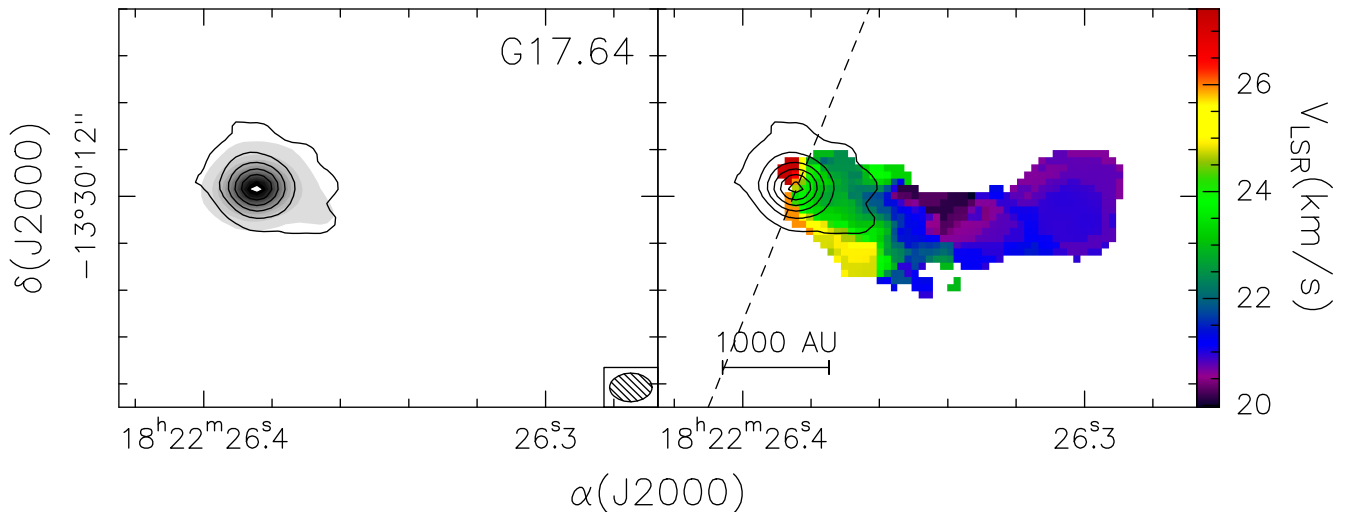
Fig. 12. Left. Contour map obtained by averaging the emission over the SiO(5–4) line from 4.0 to 39.1 km s^{-1}, overlaid on the map (grey scale) of the 1.4 mm continuum emission in G17.64. Contour levels range from 2.8 to 19.8 in steps of 3.4 mJy/beam. The synthesised beam is shown in the bottom right. **Right.** Same as left panel, overlaid on the 1st moment map of the CH$_3$CN(12–11) K=2 line. The dashed line indicates the direction of the axis of the ^{12}CO outflow detected by Kastner et al. (1994).
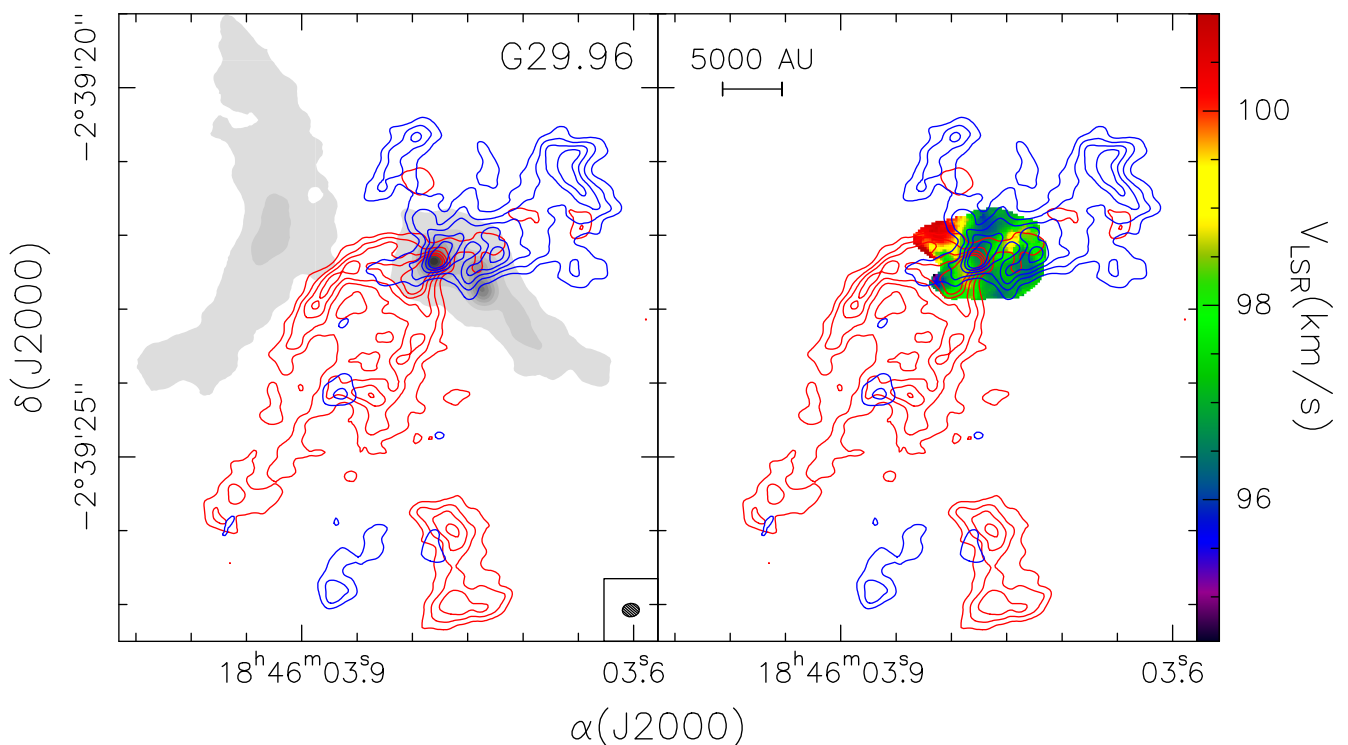
Fig. 13. Left. Contour maps of the blue- and red-shifted SiO(5–4) line emission overlaid on the map (grey scale) of the 1.4 mm continuum emission in G29.96. The SiO emission has been integrated over the velocity intervals 83.5 to 91.6 km s^{-1} and 102.4 to 110.5 km s^{-1} for the blue and red wings, respectively. Contour levels range from 6 to 26 in steps of 5 mJy/beam. The synthesised beam is shown in the bottom right. **Right.** Same as left panel, overlaid on the 1st moment map of the CH$_3$CN(12–11) K=2 line.

center of a bipolar outflow is difficult to locate with precision and we thus believe that the possibility that A1 is powering the flow cannot be ruled out. Moreover, the existence of a velocity gradient around A1 is important in itself, no matter whether this is associated with the outflow or not.

The second caveat is that the PV plot along the N–S direction across the hypercompact HII region (see Fig. 16) looks quite different from the butterfly pattern expected for rotation

speed-up toward the star ($v_{rot} \propto R^{-\alpha}$, with $\alpha > 0$). For the sake of comparison, in Fig. 16 we also plot the pattern outlining the PV plot of a Keplerian disk (i.e. $\alpha = 1/2$) rotating about a 20 $M_\odot$ star (the mass of the star ionizing the HII region; Beltrán et al. 2007). One sees an excess of emission around −1″2 and 106 km s^{-1} (indicated by the arrow in Fig. 16), which seems difficult to reconcile with the Keplerian pattern. However, it is possible that A1 is actually made of two distinct sub-cores,
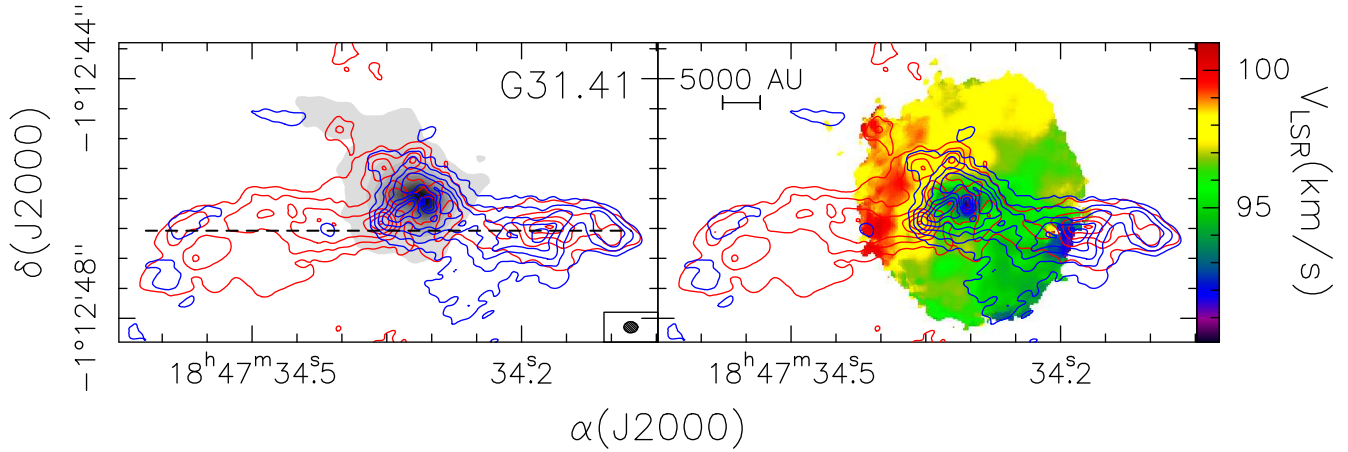
Fig. 14. Same as Fig. 13, for G31.41. The dashed line marks the axis of the SiO bipolar outflow. The SiO emission has been integrated over the velocity intervals 76.1 to 95.0 km s^{-1} and 100.4 to 119.2 km s^{-1} for the blue and red wings, respectively. Contour levels range from 7.2 to 37.2 in steps of 6 mJy/beam.
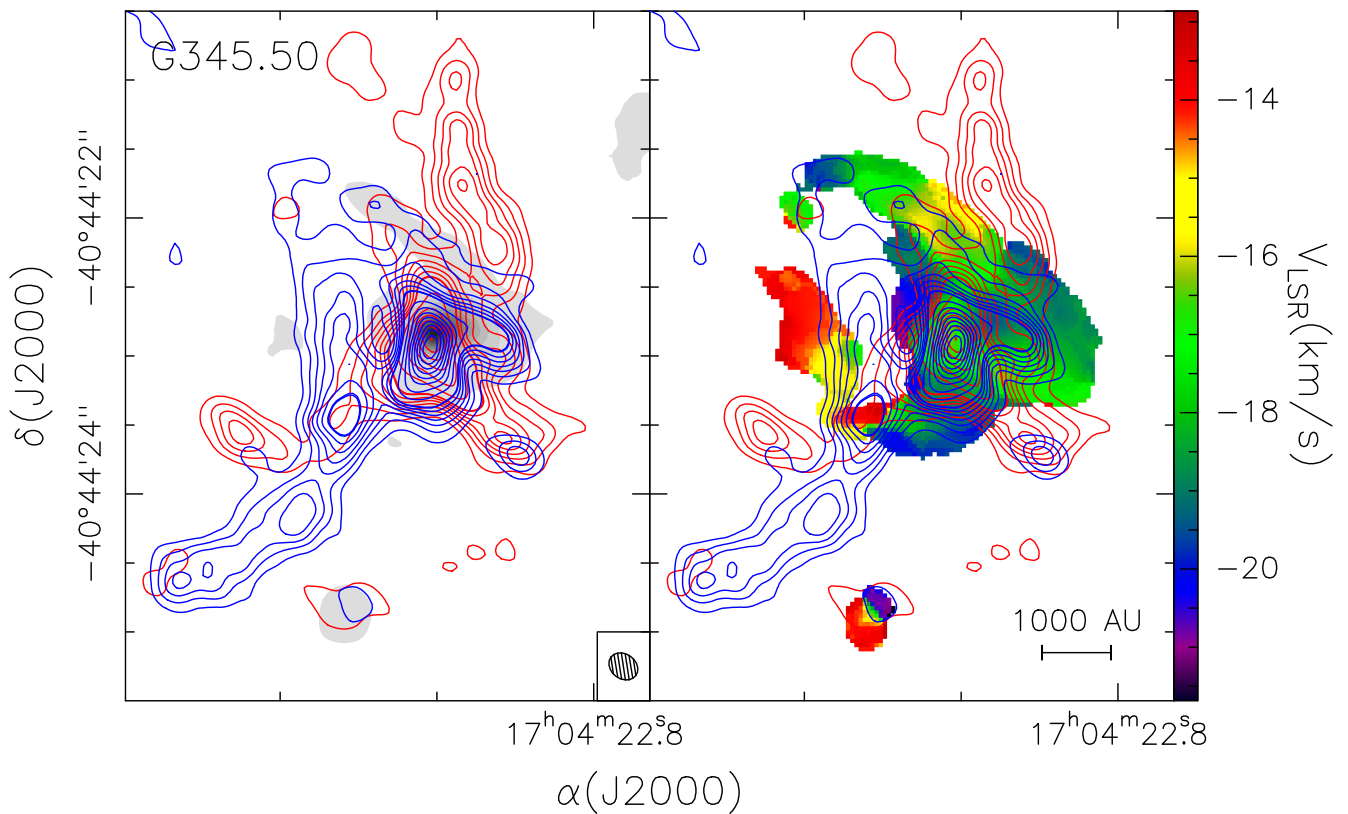

Fig. 15. Same as Fig. 13, for G345.50. The image in the right panel is the first moment of the ^{13}CH$_3$CN(13–12) K=2 line. The SiO emission has been integrated over the velocity intervals –23.8 to –18.4 km s^{-1} and –15.7 to –10.3 km s^{-1} for the blue and red wings, respectively. Contour levels range from 4.2 to 29.4 in steps of 4.2 mJy/beam and from 30 to 130.8 in steps of 12.6 mJy/beam.

as suggested by the shape of the continuum emission, which looks elongated N–S. In this case, the emission in the southern part of the disk would be contaminated by the southern sub-core. Indeed, the ^{13}CH$_3$CN PV plot (contours in Fig. 16) outlines three separate peaks, with the southern-most one (indicated by the arrow in the figure) being clearly detached from the other two, both in space (~0.′′2 or 1500 AU) and velocity (~5 km s^{-1}).

We conclude that, although speculative, the hypothesis of a Keplerian disk about a 20 $M_\odot$ star in core A1 cannot be disregarded.

5.3. G29.96

The HMC in this source lies very close to the apex of a well-known cometary UC Hɪɪ region, whose bright rim is clearly detected in our continuum map (Fig. 2). Figure 13 demonstrates
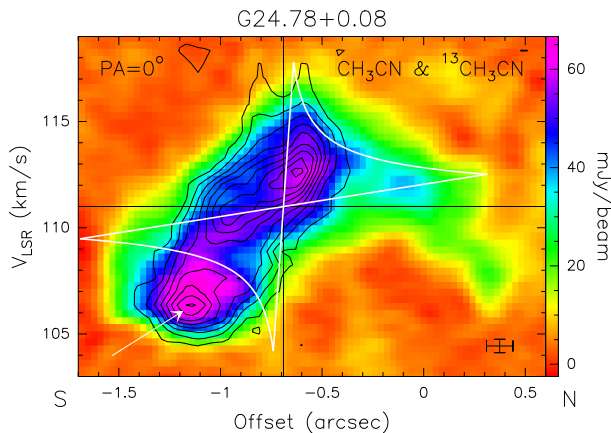
Fig. 16. Position–velocity plots of the CH$_3$CN(12–11) K=2 (colour image) and ^{13}CH$_3$CN(13–12) K=2 (contours) lines obtained along a N–S cut across the hypercompact H II region lying inside the HMC G24.78 A1 (see Beltrán et al. 2007). The offset is measured with respect to the phase center (given in Table 1). The white pattern outlines the region inside which emission is expected if the gas is undergoing Keplerian rotation about a 20 $M_\odot$ star (the mass of the O9.5 star ionizing the hypercompact H II region – see Beltrán et al. 2007), assuming edge-on inclination. The horizontal and vertical lines mark, respectively, the position of the H II region and the systemic LSR velocity. The cross in the bottom right indicates the angular and spectral resolution. The arrow points at the emission peak probably associated with a secondary sub-core.

that the velocity gradient observed in CH$_3$CN is approximately perpendicular to the SiO bipolar outflow that emerges from the HMC itself. We thus consider the PV plot along a direction with PA=52°, passing through the HMC.

As one can appreciate in Fig. 17, this plot is roughly consistent with the butterfly-shaped emission expected for rotation about the outflow axis with $v_{rot} \propto R^{-\alpha}$. In particular, the white Keplerian pattern in the figure corresponds to a central mass of 10 $M_\odot$. Note that this is shown only for the sake of comparison and *not* a fit to the data. When comparing this pattern with the observed emission, one must take into account that the former assumes and edge-on geometry, zero line width, and infinite angular resolution. Moreover, it does not include a radial component of the velocity, due to infall, which is suggested by the inverse P-Cygni profile detected in the ^{13}CO(2–1) line by Beltrán et al. (2011a). Multiplicity may also disturb the velocity field, as shown by Beuther et al. (2007), who resolved the main core into substructures. Therefore, a precise estimate of the stellar mass from the PV plot requires fitting the data with a disk model such as that by Johnston et al. (2015), which takes into consideration also the inclination of the disk with respect to the line of sight[6].

5.4. G31.41

The literature about this HMC is very rich (see e.g. Cesaroni et al. 1994b, 2010, Moscadelli et al. 2013, Mayen-Gijon et al. 2014, and references therein). In particular, previous

---

[6] We stress that the dynamical mass, derived for the central star assuming an edge-on Keplerian disk, is a lower limit.
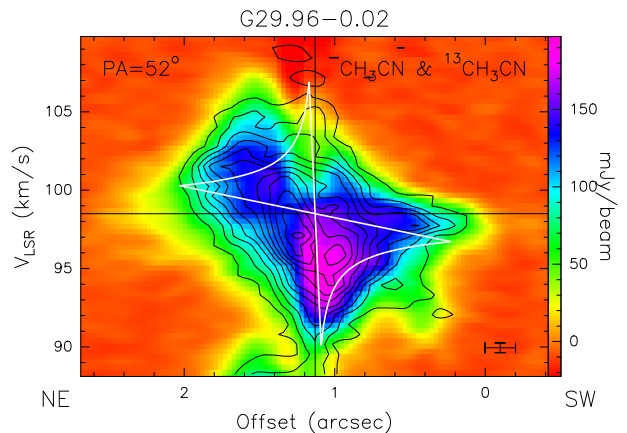

Fig. 17. Same as Fig. 16, for the HMC in G29.96. The cut is made through the HMC along PA=52°(dotted line in Fig. 8). The white pattern corresponds to Keplerian rotation about a 10 $M_\odot$ star.

IRAM-PdBI (Beltrán et al. 2004, 2005) and SMA (Cesaroni et al. 2011) observations have confirmed the existence of a clear velocity gradient in CH$_3$CN directed approximately NE–SW, but could not establish the presence of an outflow associated with the core. The CO(2–1) line maps by Cesaroni et al. (2011) suggested the existence of a bipolar symmetry in the E–W direction roughly centered on the HMC, but the confusion with emission from the envelope and perhaps from unassociated gas along the line of sight made it difficult to draw any conclusion.

The new ALMA data represent an increase by a factor ∼4 in angular resolution and provide us with a more selective jet/outflow tracer (i.e. SiO). The main findings can be summarized as follows:

– Albeit well resolved, the continuum emission unveils a very smooth structure of the HMC, without any hint of fragmentation (Fig. 2). However, such a simple structure does not necessarily mirror the real structure of the core, because the continuum emission at 1.4 mm is in all likelihood optically thick, as suggested by the large value of the peak brightness temperature (∼130 K), the highest of our sample. Such a large opacity/brightness explains the existence of deep absorption even in CH$_3$CN lines with excitation as high as ∼200 K (see Fig. 18), which in turn is responsible for the dip at the center of the ring-like maps in the left panels of Fig. 9.
– The velocity of the gas increases smoothly from SW to NE (Fig. 9). However, the study of the velocity field on a small scale is hindered by the large continuum opacity close to the core center. This prevents us from inspecting the kinematics of the central region, where any putative sign of Keplerian-like rotation could be detected.
– All CH$_3$CN lines (as well as many others) present inverse P-Cygni profiles (see Fig. 18) towards the core center, an strong indication of infall. This is why the velocity at the center of the 1st moment map in Fig. 9 appears blue shifted. The presence of infall is relevant to the existence of a disk in that it could affect its structure and stability, depending on the ratio between the rotation period and accretion time scale (see Fig. 14 of Beltrán & de Wit 2016).
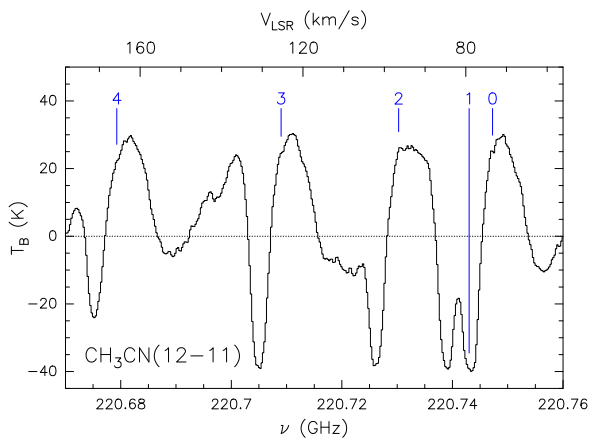
Fig. 18. Spectrum of the CH$_3$CN(12–11) K=2 to 4 lines towards the absorption dip of the G31.41 HMC. The vertical lines mark the different K components. The LSR velocity given in the upper x-axis refers to the K=2 component. Note the inverse P-Cygni profiles of all lines, except the K=1 component, which is heavily blended with the K=0.

– A clear bipolar outflow is detected in the SiO(5–4) line (Fig. 14). The blue and red lobes lie on the same side as the CH$_3$CN blue- and red-shifted emission. However, the direction of the CH$_3$CN velocity gradient (PA≃68°) is significantly different from that of the outflow axis (PA≃0°; see Fig. 9) and the geometrical center of the outflow is offset by ∼0.″65 to the south with respect to the HMC center (see Figs. 9 and 14). Therefore, we do not believe that the SiO outflow and the CH$_3$CN velocity gradient are due to the same phenomenon and associated with the same source.

With this in mind, we study the PV plot along the direction with PA=68° passing through the HMC. In order to minimize the effect of the absorption towards the core center, we average the emission along the direction perpendicular to the cut of the PV plot. Moreover, since the CH$_3$CN lines are heavily affected by the absorption, we prefer to use the isotopologue ^{13}CH$_3$CN.

We compare the PV plot of the ^{13}CH$_3$CN(13–12) K=2 transition in Fig. 19a, with the same plot of the CH$_3$CN(12–11) v_8=1 K,l=6,1 line in Fig. 19b. The striking result is that the slope of the emission is steeper in the v_8 = 1 line. Since the gas temperature is expected to increase towards the core center and the v_8=1 transition has a greater excitation energy (778 K) than the ground state line (96 K), the different slopes indicate that at smaller radii the gas velocity increases. In other words, the higher the excitation of a line, the closer to the core center the line will be observed, and Fig. 19 shows that getting close to the center the gas has also higher velocity. This result is consistent with $v_{rot} \propto R^{-\alpha}$. Indeed, the same type of "steepening" of the PV plot with increasing energy of the transition can be seen in Fig. 4 of Johnston et al. (2015), where the observed PV plots are fitted with a disk undergoing Keplerian rotation.

With all the caveats previously discussed and related to the large continuum opacity and presence of absorption, we believe that our findings are consistent with a scenario where the gas in G31.41 is rotating and infalling towards the core center with conservation of angular momentum, and eventually accreting onto one or more stars through a circumstellar disk.
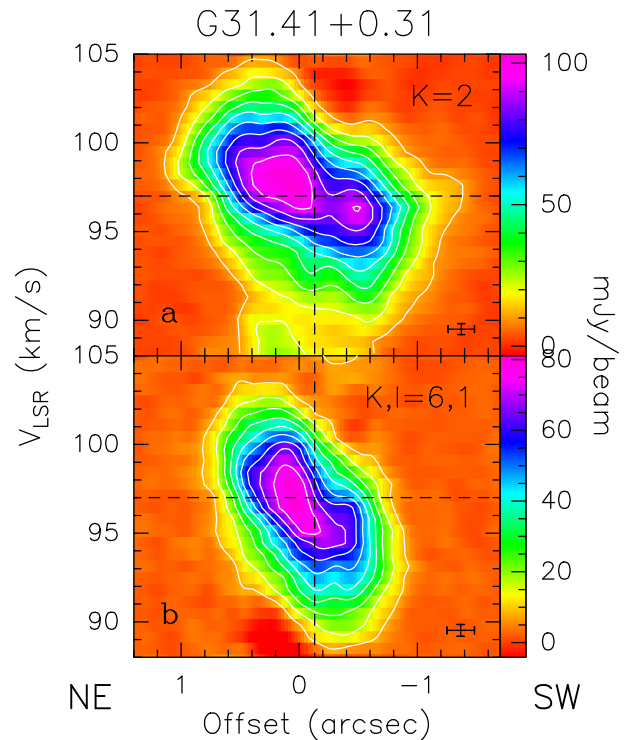

Fig. 19. a. PV plot of the ^{13}CH$_3$CN(13–12) K=2 line emission (excitation energy of 96 K) in G31.41 along a direction with PA=68° passing through the HMC (dotted line in Fig. 9). The vertical and horizontal dashed lines indicate, respectively, the position of the continuum peak and the systemic velocity. The cross in the bottom right denotes the angular and spectral resolutions. **b.** Same as top panel, for the CH$_3$CN(12–11) v_8=1 K,l=6,1 line (excitation energy of 778 K).

5.5. G345.49

Although several cores are present within the primary beam of our ALMA observations, we have chosen to focus on the strongest continuum source, M, which lies at the center of the thermal radio jet observed by Guzmán et al. (2010, 2016). The central radio source and the direction of the jet axis are denoted in Fig. 10 with a cross and a dashed line, respectively. Comparison between the jet direction and the 1st moment map indicates that CH$_3$CN is tracing expansion along the jet. However, the velocity gradient is not exactly directed along the jet axis, but appears to have a component in the perpendicular direction as well. The PV plot in Fig. 20 has been obtained along the direction with PA=+15°, i.e. perpendicular to the jet axis, through the continuum peak. In order to maximize the signal-to-noise, the emission has also been averaged over a stripe spanning ±0.″25 across the cut. Note that the corresponding PV plot for the ^{13}CH$_3$CN(13–12) line cannot be used, because the emission is barely detected (see Fig. 10).

The CH$_3$CN emission in Fig. 20 appears to trace only half of the butterfly-shaped pattern expected for Keplerian rotation about a 10 $M_\odot$ star, as the red-shifted "wing" is missing. Such an incomplete structure is not surprising, as the presence of a strong free-free source suggests that the onset of a hypercompact H$_{II}$ region at the jet center could have deeply perturbed the disk morphology. Besides, significant deviations from axial symmetry are indeed predicted by numerical simulations
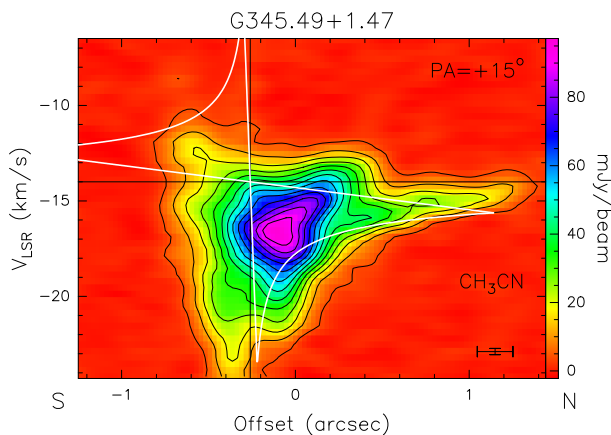
Fig. 20. PV plot of the $CH_3CN(12–11)$ K=2 line emission (colour scale and contours) for G345.49 M. The cut is made through the strongest continuum peak, along PA=15°. Unlike the PV plots of the other sources, here we do not plot the $^{13}CH_3CN(13–12)$ emission since it is barely detected (see Fig. 10). The white pattern corresponds to Keplerian rotation about a 10 $M_\odot$ star.

(Krumholz et al. 2007b; Peters et al. 2010, 2011; Kuiper et al. 2011; Klassen et al. 2016).

5.6. G345.50

This source lies at the center of a bipolar nebula oriented approximately NE–SW, which can be seen at IR wavelengths in the Spitzer/GLIMPSE images (Churchwell et al. 2009). While the focus of the observations was on the main core at the center of the field covered by ALMA, a southern core was serendipitously detected. We will refer to the main and southern cores, respectively, as G345.50 M and G345.50 S (see Fig. 2).

Both cores are detected in the CH_3CN and $^{13}CH_3CN$ lines, which trace clear velocity gradients directed roughly E–W (for G345.50 M) and N–S (for G345.50 S). This can be seen in Fig. 11 and even more clearly for source M in Fig. 21, where the first moment map has been clipped outside the border of the core, namely outside the 5σ contour level of the continuum emission. Further analysis of the velocity field is presented in Figs. 22 and 23, where we show the PV plots of the $CH_3CN(12–11)$ K=2 line along suitable directions across the two cores. As done for the other sources, we show the pattern expected for Keplerian rotation about a 10 $M_\odot$ star. Remarkably, both plots present a butterfly shape, consistent with an increase of the rotation velocity towards the center. As already pointed out, an estimate of the central point mass is hazardous without a model fit. However, the main difference between the two PV plots is mostly due G345.50 M having a more irregular shape, whereas the range in velocity is basically the same as for G345.50 S.

One may speculate that the mass of the two stars is basically the same and the different shape of the PV plots could depend on the surrounding environment, with G345.50 S being more isolated and hence less perturbed, for instance, by interactions with a (deeply embedded) stellar cluster. In this scenario, G345.50 M would be closer to the center of the gravitational potential well and thus could have evolved faster, warming up
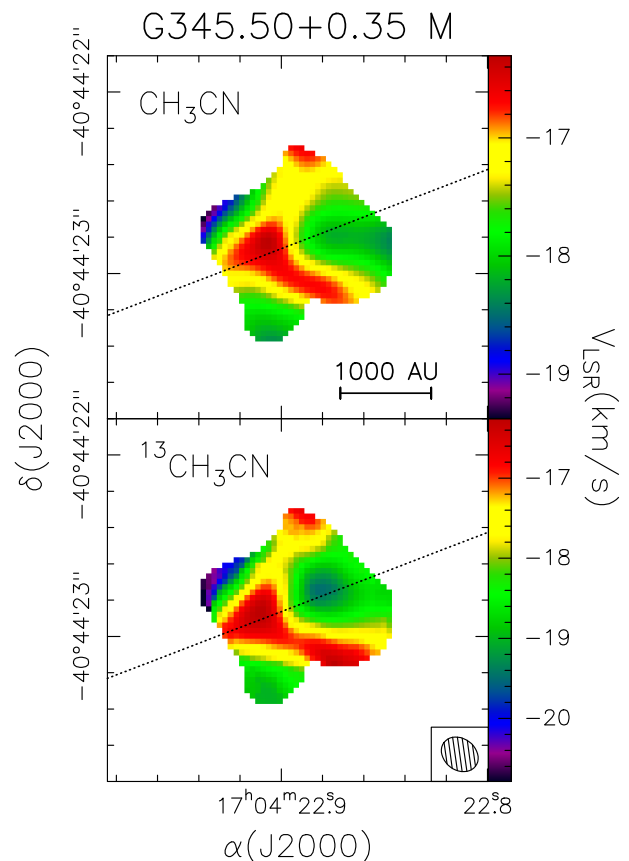

Fig. 21. First moment map of the $CH_3CN(12–11)$ K=2 (top panel) and $^{13}CH_3CN(13–12)$ K=2 (bottom) lines towards the HMC in G345.50 M. The data have been clipped outside the 5σ contour level of the continuum emission to show the velocity gradient along the direction denoted by the dotted line. The synthesised beam is shown in the bottom right.

the surrounding material. The combination of infall and outflow could be the reason that the structure is so complex. Vice versa, S would have formed later and/or have a lower accretion rate, with less impact on its surroundings, which are less complex due to simpler dynamics.

The morphology of the SiO(5–4) line emission appears much more complex than in other sources (see Fig. 15). The blue- and red-shifted emissions outline two elongated structures on opposite sides with respect to G345.50 M, but no obvious symmetry axis can be identified. In the case of G345.50 S, the SiO emission is very faint and no clear pattern can be recognized. It is thus difficult to establish whether a bipolar outflow (possibly related to the large-scale bipolar nebula seen at IR wavelengths) is present in this field. It must be noted though that the location of the blue-shifted gas, on the eastern side, coincides with the IR reflection nebula, consistent with seeing more scattered light from the lobe facing the observer. In contrast, most of the IR nebulosity on the western side is due to the extended cometary H II region imaged in the radio by Garay et al. (2006), and is hence not tracing the red lobe of the (putative) outflow.
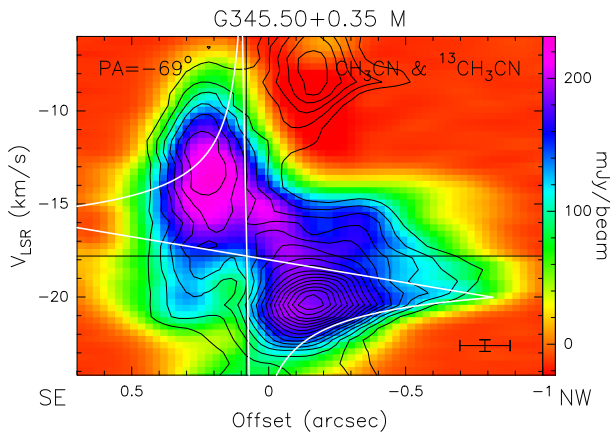
Fig. 22. Same as Fig. 17, for the HMC in G345.50 M. The cut is made through the HMC along PA=−69°(dotted line in Fig. 11). Note that the peak at –0.″15 and –8 km s^{-1} of the contour map is due to emission in an unidentified molecular line.
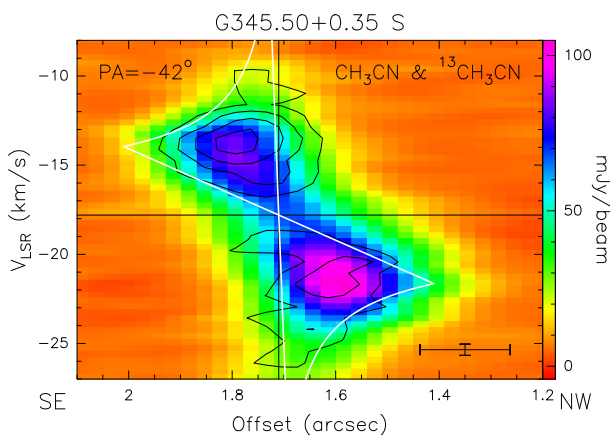

Fig. 23. Same as Fig. 17, for the HMC in G345.50 S. The cut is made through the HMC along PA=−42°(dotted line in Fig. 11).

Fig. 24. Same as Fig. 19, for the HMC in G24.78 A1.

6. Discussion: Are there disks around O-type stars?

As previously explained, the goal of our project was to establish whether circumstellar disks are present around O-type (proto)stars. Has our search been successful? Based on the results discussed in the previous sections, we can state that we find evidence for rotation in at least 3 cases (G29.96, G345.50 M, G345.50 S), plus 3 additional candidates (G24.78, G31.41, G345.49), albeit more questionable. Such evidence is based on the existence of velocity gradients across molecular cores. Above we have discussed the interpretation of these gradients in terms of rotation. While the fingerprint of Keplerian-like rotation is the butterfly shape of the PV plots (see Sect. 5), it is also useful to compare the PV plots of lines with different excitation energies, as done for G31.41 (see Fig. 19). Since the temperature is expected to be higher close to the core center, where the gas rotates faster (because $v_{rot} \propto R^{-\alpha}$), then for increasing line energy the emission peak in the PV plot should move towards more extreme blue- and red-shifted velocities (see Sect. 5.4).
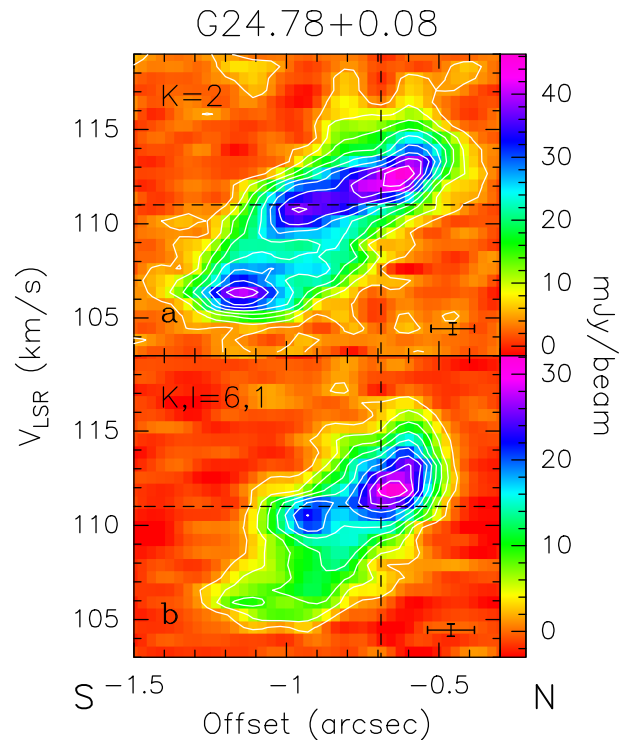
On the analogy of the analysis of G31.41, we thus compare the PV plot of the $^{13}CH_3CN(13–12)$ $K=2$ line with that of a vibrationally excited line, for all other cores where velocity gradients have been detected. Only for source G345.49 the CH_3CN line was used instead of the $^{13}CH_3CN$ transition, because the latter is undetected towards the core (see Fig. 10). The results are shown in Figs. 24 to 28. Although less remarkable than for G31.41, a significant difference is seen between the PV plots in the two lines, for G29.96, G345.50 M, and G345.50 S. In fact, dividing the PV plot in the bottom panel by that in the top panel, one sees that in these objects the highest ratio between the vibrationally excited line and the ground state line is found close to the continuum peak and at relatively large velocity offsets, as expected for rotation speed-up towards the center (see the discussion on G31.41 in Sect. 5.4). In particular, in G29.96 the maximum ratio is found at 0.″9 and 91.5 km s^{-1}, in G345.50 M at –0.″1 and –23.3 km s^{-1}, and in G345.50 S at 1.″6 –25 km s^{-1}. These results are consistent with the emission extending to higher velocities in the higher excitation line. While other interpretations are possible, these findings are consistent with these three sources undergoing Keplerian-like rotation.

Table 4 summarizes our conclusions for the different targets, whose distance, spatial resolution, and L_{bol}/M_{gas} ratio are also given. For the sake of comparison, we have included also the AFGL 4176 disk, detected by Johnston et al. (2015), the only bona-fide disk around an O-type star known to date. We find some evidence consistent with the presence of a disk in all sources but G17.64. Note that we refer to the *molecular* component of the disk, whose absence does *not* rule out the presence of, e.g. an ionized disk or any other disk-like structure detectable in other tracers than those adopted here.
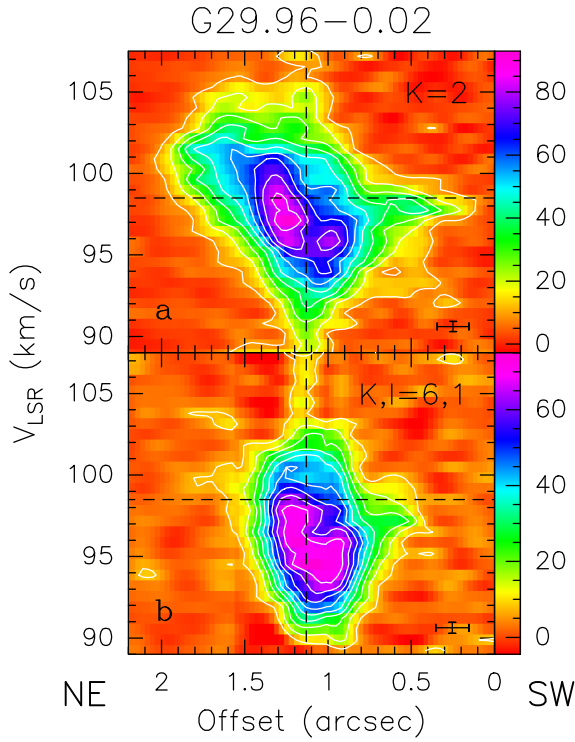
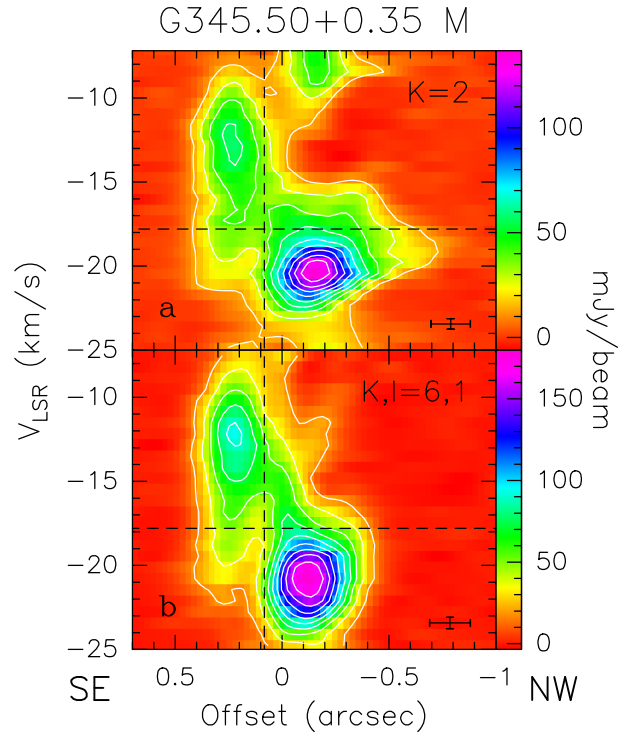**Fig. 25.** Same as Fig. 19, for the HMC in G29.96.
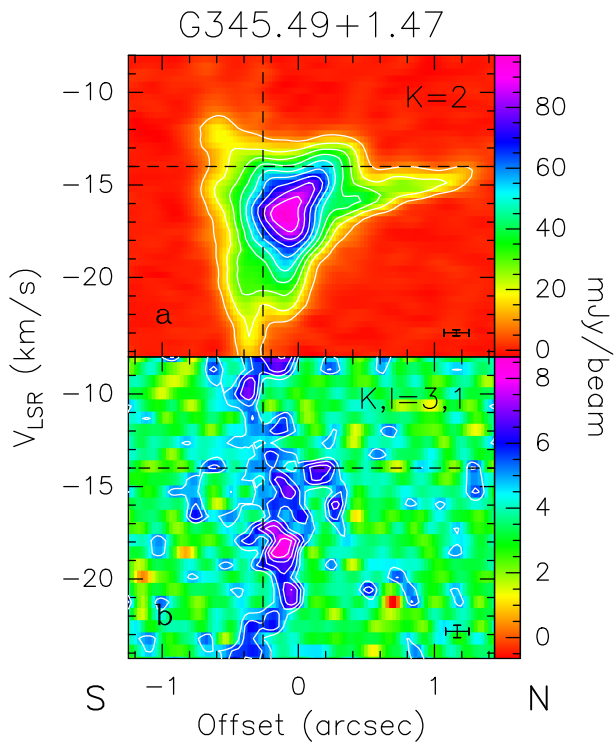

Fig. 26. Same as Fig. 19, for the G345.49 M and the CH$_3$CN(12–11) K=2 and v_8=1 K,l=3,1 lines.
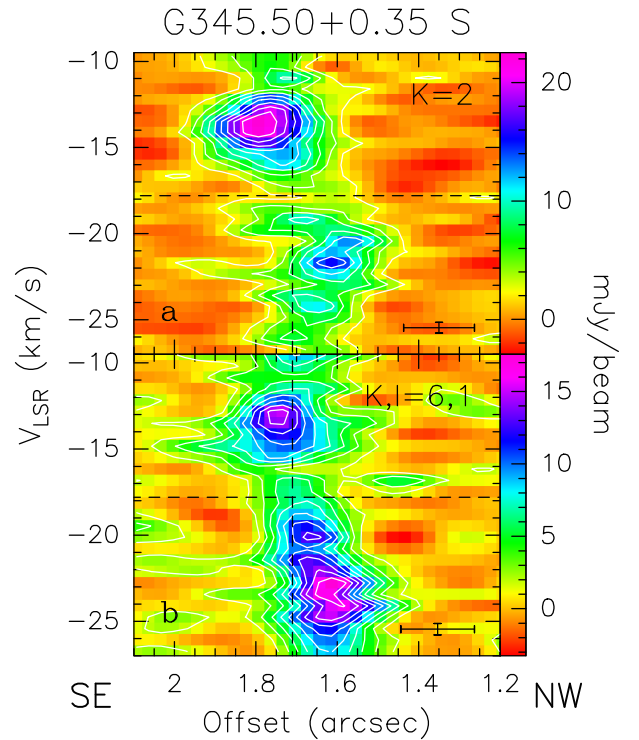

Fig. 27. Same as Fig. 19, for G345.50 M.

Fig. 28. Same as Fig. 19, for G345.50 S.

The results of Table 4 are visually represented in Fig. 29, where we plot the $L_{\rm bol}/M_{\rm gas}$ ratio as a function of distance. A few considerations are in order.

One sees that the most evolved source (i.e. the one with the highest value of $L_{\rm bol}/M_{\rm gas}$), G17.64, is also the only source

without evidence for rotation. We remind the reader that the estimate of $L_{\rm bol}/M_{\rm gas}$ for G29.96 is an upper limit due to the presence of the star ionizing the nearby UC HII region (see Sect. 2); therefore the core is likely younger than suggested by the value of $L_{\rm bol}/M_{\rm gas}$. Although some hint of a disk seems present in the youngest sources (G31.41 and G24.78), the best disk

Table 4. Properties of the cores with velocity gradients detected with ALMA.

Name	d	HPBW[a]	L_{bol}/M_{gas}	disk[b]
	(kpc)	(AU)	$(L_\odot/M_\odot)$	
G17.64+0.16	2.2	332	300	N
G24.78+0.08 A1	7.7	1205	15	?
G29.96−0.02 HMC	5.26	1168	300[c]	Y
G31.41+0.31	7.9	1707	17	?
G345.49+1.47 M	2.4	483	22	?
G345.50+0.35 M	2.0	402	84	Y
G345.50+0.35 S	2.0	1217	84	Y
AFGL 4176[d]	*4.2*	*1205*	*120*	*Y*

[a] Half-power width of the synthesised beam at the distance of the source.

[b] Y=disk candidate; ?=questionable disk; N=no evidence for a molecular disk.

[c] Note that a significant fraction of L_{bol} from G29.96 is known to be contributed by the O5–O6 star associated with the nearby UC Hɪɪ region (see Sect. 2).

[d] Revealed with ALMA by Johnston et al. (2015). The values of L_{bol} (1.7×10^5 $L_\odot$) and M_{gas} (1400 $M_\odot$) have been taken from Beltrán et al. (2007), after correcting for the different distance (4.7 kpc instead of 5.3 kpc) and dust temperature (50 K instead of 30 K).
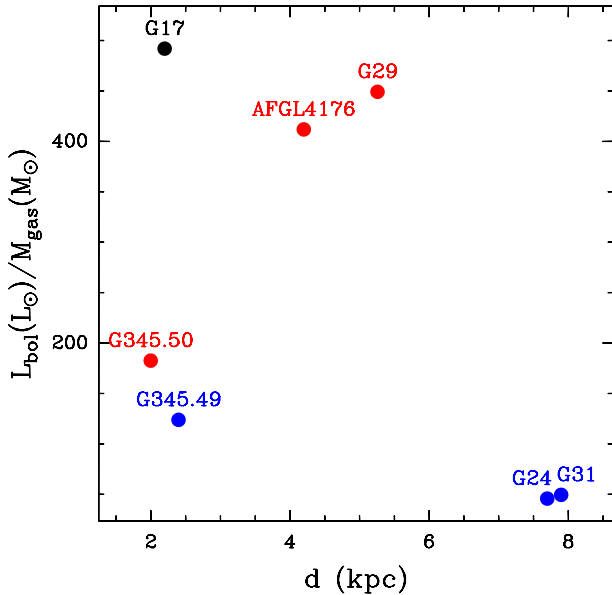

Fig. 29. Luminosity-to-mass ratio versus source distance for the 6 targets of our sample plus the disk around the 25 $M_\odot$ star in AFGL 4176 detected by Johnston et al. (2015). Black, red, and blue points indicate, respectively, sources without evidence for disks, with disk candidates, and with questionable disk candidates (see Table 4).

candidates are G29.96, the two in G345.50, and, obviously, AFGL 4176, which have intermediate values of L_{bol}/M_{gas}.

The (apparent) lack of disks at a relatively later evolutionary stage is not surprising, because our observations make use of high density tracers, and the densest gas is gradually dispersed on a relatively large scale during the early evolution of a massive YSOs. Conversely, the marginal detection of disks in the youngest sources might be due to the massive envelopes enshrouding the newly born stars; as discussed for G31.41

(see Sect. 5.4), their large opacity could confuse the picture and make it difficult to distinguish the embedded circumstellar disks. Also, stable Keplerian disks may start small and grow up with time, as suggested for low-mass stars where only few disks have been detected around Class 0 objects (Tobin et al. 2015; Murillo et al. 2013).

In this scenario, the best targets for our search are those YSOs where the molecular component of the disk is still important, but the surrounding envelope is less prominent. In fact, the influence of the environment has been discussed in Sect. 5.6: the disk around G345.50 M appears much more perturbed (and hence more difficult to identify) than that around G345.50 S, because in the latter the circumstellar matter has a less complex distribution. In addition, as also discussed in Sect. 5.6, an age effect could be present, because younger disks could be too small, making their detection challenging even for ALMA.

The previous considerations do not take into account another crucial parameter: the source distance. For obvious reasons one would expect the disk detection rate to decrease with increasing distance. As a matter of fact, if G345.50 were located, e.g., at 7 kpc, the velocity gradient could still be detected, but the butterfly-shape of the PV plot in Fig. 23 would not be recognizable. This is demonstrated by Fig. 30, where the angular resolution of the original data has been degraded by a factor 3.5 (i.e. the ratio between 7 kpc and the distance of G345.50, 2 kpc). Nevertheless, no obvious dependence of the detection rate with distance is seen in Table 4 and Fig. 29. In contrast, the only source (G17.64) without any evidence for a disk (from our ALMA data) is one of the closest, while one of the best candidates (G29.96) lies beyond 5 kpc.

With the caveat that the previous analysis is based on very low-number statistics and a much larger number of cases has to be studied to reach statistical significance, we conclude that the detectability of a circumstellar disk around an O-type star appears sensitive to the evolutionary stage of the YSO. Under this hypothesis, the relatively low disk detection rate obtained in our observations is mostly due to the evolutionary phase of our targets: too late and too early are both unsuited – albeit for opposite reasons – and make it difficult to obtain a clear disk detection. This apparently negative argument can be converted into a positive one: *if circumstellar disks are found at an intermediate evolutionary stage, they are likely to exist also in younger objects and thus be widespread in these luminous YSOs.*

It remains to be understood if the stars at the center of our disk candidates are indeed massive enough to be classified as O-type stars and if the gas mass is consistent with Keplerian-like rotation.

Visual comparison between the PV plots and the white patterns[7] corresponding to Keplerian rotation (see Figs. 16–23) suggests that a stellar mass of ∼10 $M_\odot$ might suffice. This may be even less if stellar multiplicity is present, as expected for such luminous objects. However, a similar approach applied to the disk in AFGL 4176 studied by Johnston et al. (2015) suggests a stellar mass ≲10 $M_\odot$, significantly less than that ob-

---

[7] These patterns can be obtained, e.g., from Eq (1) of Cesaroni et al. (2011), where only the rotation term must be considered.
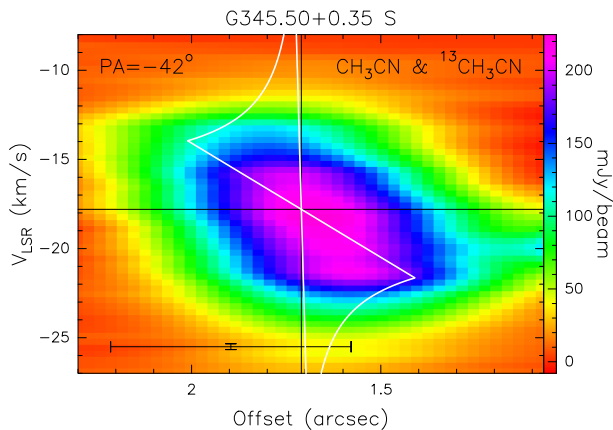
Fig. 30. Same as Fig. 23 for the CH$_3$CN(12–11) K=2 line in G345.50, after degrading the angular resolution by a factor 3.5.

tained from their model fit (25 $M_\odot$). Moreover, if the disk is not edge-on the dynamical mass is a lower limit. For these reasons, we conclude that our findings are consistent with the detection of disks around stars in excess of 10 $M_\odot$. To base this conclusion on a solid ground and, at the same time, obtain a precise estimate of other important parameters such as the disk mass, model fits analogous to that of Johnston et al. (2015) will be needed, a goal beyond the scope of the present study.

Finally, it is worth noting that to allow for Keplerian-like rotation, the disk mass should not exceed the stellar mass. It is thus important to verify that the masses of our cores are not much greater than any plausible stellar mass. An estimate of the gas mass can be obtained from the continuum emission if one knows the dust temperature. The latter could be obtained by fitting the line emission of HMC tracers such as CH$_3$CN, under the assumption of equal gas and dust temperatures. A correct analysis should take into account also the existence of temperature gradients both in the (putative) disk and the surrounding envelope. While all this requires complex modelling, we may obtain a rough estimate of the mass using a plausible temperature from previous observations of some of our sources. For example, in G24.78 and G31.41 Beltrán et al. (2005) derive temperatures spanning from 60 K to 350 K. For our sources, we assume a fiducial value of 200 K, a dust absorption coefficient $\kappa_{dust} = 1$ cm^{2}g^{-1} at 1.4 mm (Ossenkopf & Henning 1994), and a gas-to-dust mass ratio of 100. One obtains gas masses ranging from 0.09 $M_\odot$ to 330 $M_\odot$, with only one source, G31.41, exceeding 19 $M_\odot$. In conclusion, in all cases, apart from G31.41, the gas mass is sufficiently small to warrant Keplerian rotation about a putative embedded O-type star. The exceptionally large size of the core in G31.41 (see Fig. 3) suggests that the estimated core mass of 330 $M_\odot$ is probably dominated by the envelope, which is very difficult to separate from any embedded disk.

7. Summary and conclusions

We have reported on the results of ALMA observations of continuum and molecular line emission towards a selected sample of 6 high-mass star forming regions with luminosities typical of O-type stars. Our goal was to establish whether circumstel-

lar disks around these stars are as common as in lower-mass YSOs. After analysing the CH$_3$CN and ^{13}CH$_3$CN lines and (in 3 targets) the associated SiO line emission in the six regions, we find that in five of these at least one disk candidate is found and in two cases a clear bipolar outflow can be recognised.

The limited number of outflow detections suggests that in these massive objects collimated jets might be rare – perhaps short-lived – and the ejection phenomenon could be dominated by wide-angle winds, mostly resolved out in our high-resolution images. Whether this is an effect of age, intrinsic decollimation, precession, or presence of multiple stars cannot be decided on the basis of our data.

Further analysis of the velocity field by means of PV plots shows that in 3 objects a butterfly-shaped pattern is recognisable, which is believed to be a signpost of Keplerian-like ($v_{rot} \propto R^{-\alpha}$, with $\alpha > 0$) rotation, whereas in the other 3 cores only marginal evidence for that is seen.

With the caveat that a larger number of objects has to be studied to base any final statement on a solid statistical ground, we conclude that unveiling the presence of circumstellar disks around O-type stars may be extremely challenging even for ALMA, because young, deeply embedded disks may be masked by the surrounding optically thick envelope, while evolved ones could have lost most of their molecular component. Only disks around YSOs in an intermediate evolutionary phase could be detectable. In this respect, the study of more complex molecules, with lower abundances than CH$_3$CN and its isotopologues, could help tracing the disk, thanks to their (presumably) lower line opacities.

The lesson to learn from our findings is that too young and too old are both unsuited, and future searches for disks around young O-type YSOs should take this caveat into consideration.

References

Bachiller, R. & Pérez Gutiérrez, M. 1997, ApJ, 487, L93
Beltrán, M.T., Cesaroni, R., Neri, R., et al. 2004, ApJ, 601, L187
Beltrán, M.T., Cesaroni, R., Neri, R., et al. 2005, A&A, 435, 901
Beltrán, M.T., Brand, J., Cesaroni, R., et al. 2006, A&A, 447, 221
Beltrán, M.T., Cesaroni, R., Moscadelli, L., & Codella, C. 2007, A&A, 471, L13

Beltrán, M.T., Cesaroni, R., Neri, R., & Codella, C. 2011a, A&A, 525, A151

Beltrán, M.T., Cesaroni, R., Zhang, Q., et al. 2011b, A&A, 532, A91

Beltrán, M.T., Olmi, L., Cesaroni, R., et al. 2013, A&A, 552, A123

Beltrán, M.T., Sánchez-Monge, Á., Cesaroni, R., et al. 2014, A&A, 571, A52

Beltrán, M.T. & de Wit, W.J. 2016, A&ARv, 24, 6

Beuther, H., Zhang, Q., Bergin, E.A., et al. 2007, A&A, 468, 1045

Bonnell, I.A. & Bate, M.R. 2006, MNRAS, 370, 488

Cesaroni, R., Neri, R., Olmi, L., et al. 2005, A&A, 434, 1039

Cesaroni, R., Beltrán, M.T., Zhang, Q., Beuther, H., & Fallscheer, C. 2011, A&A, 533, A73

Cesaroni, R., Galli, D., Neri, R., & Walmsley, C.M. 2014, A&A, 566, A73

Cesaroni, R., Churchwell, E., Hofner, P., Walmsley, C.M., & Kurtz, S. 1994a, A&A, 288, 903

Cesaroni, R., Olmi, L., Walmsley, C.M., Churchwell, E., & Hofner, P. 1994b, ApJ, 435, L137

Cesaroni, R., Galli, D., Lodato, G., Walmsley, C.M., & Zhang, Q. 2007, in Protostars and Planets V, ed. B. Reipurth, D. Jewitt, & K. Keil (Tucson: Univ. of Arizona Press), 197

Cesaroni, R., Hofner, P., Araya, E., & Kurtz, S. 2010, A&A, 509, 50

Cesaroni, R., Pestalozzi, M., Beltrán, M.T., et al. 2015, A&A, 579, A71

Codella, C., Beltrán, M.T., Cesaroni, R., et al. 2013, A&A, 550, A81

Condon, J.J., Cotton, W.D., Greisen, E.W., et al. 1998, AJ, 115, 1693

Contreras, Y., Schuller, F., Urquhart, J. S., et al. 2013, A&A, 549, A45

Churchwell, E., Babler, B.L., Meade, M.R., et al. 2009, PASP, 121, 213

De Buizer, J.M., Watson, A.M., Radomski, J.T., Piña, R.K., & Telesco, C.M. 2002, ApJ, 564, L101

Elia, D., Schisano, E., Molinari, S., et al. 2010, A&A, 518, L97

Faúndez, S., Bronfman, L., Garay, G., et al. 2004, A&A, 426, 97

Forster, J.R. & Caswell, J.L. 1989, A&A, 213, 339

Garay, G., Brooks, K.J., Mardones, D., & Norris, R.P. 2006, ApJ, 651, 914

Gueth, F., Guilloteau, S., & Bachiller, R. 1998, A&A, 333, 287

Ginsburg, A., Glenn, J., Rosolowsky, E., et al. 2013, ApJS, 208, 14

Guzmán, A.E., Garay, G., Brooks, K.J. 2010, ApJ, 725, 734

Guzmán, A.E., Garay, G., Brooks, K.J., Rathborne, J., & Güsten, R. 2011, ApJ, 736, 150

Guzmán, A.E., Garay, G., Rodríguez, L.F., et al. 2016, ApJ, 826, 208

Johnston, K.G., Robitaille, T.P., Beuther, H., et al. 2015, ApJ, 813, L19

Kastner, J.H., Weintraub, D.A., Snell, R.L., et al. 1994, ApJ, 425, 695

Keto, E. 2002, ApJ, 580, 980

Keto, E. 2003, ApJ, 599, 1196

Keto, E. 2007, ApJ, 666, 976

Klassen, M., Pudritz, R.E., Kuiper, R., Peters, T., & Banerjee, R. 2016, ApJ, 823, 28

Krumholz, M.R., Klein, R.I., & McKee, C.F., 2007a, ApJ, 656, 959

Krumholz, M.R., Klein, R.I., & McKee, C.F., 2007b, ApJ, 665, 478

Krumholz, M.R., Klein, R.I., McKee, C.F., Offner, S.S.R., & Cunningham, A.J. 2009, Science, 323, 754

Kuiper, R., Klahr, H., Beuther, H., & Henning, Th. 2010, ApJ, 722, 1556

Kuiper, R., Klahr, H., Beuther, H., & Henning, Th. 2011, ApJ, 732, 20

Kuiper, R., Turner, N.J., & Yorke, H.W. 2016, ApJ, 832, 40

Lumsden, S.L., Hoare, M.G., Urquhart, J.S., et al. 2013, ApJS, 208, 11

Martín-Hernández, N.L., Bik, A., Kaper, L., Tielens, A.G.G.M., & Hanson, M.M. 2003, A&A, 405, 175

Maud, L.T., Lumsden, S.L., Moore, T.J.T., et al. 2015a, MNRAS, 452, 637

Maud, L.T., Moore, T.J.T., Lumsden, S.L., et al. 2015b, MNRAS, 453, 645

McKee, C. F. & Tan, J. C. 2003, ApJ, 585, 850

Mayen-Gijon, J.M., Anglada, G., Osorio, M., et al. 2014, MNRAS, 437, 3766

Menten, K.M. & van der Tak, F.F.S. 2004, A&A, 414, 289

Moisés, A.P., Damineli, A., Figuerêdo, E., et al. 2011, MNRAS, 411, 705

Molinari, S., Swinyard, B., Bally, J., et al. 2010, PASP, 122, 314

Molinari, S., Schisano, E., Elia, D., et al. 2016, A&A, 591, A149

Moscadelli, L., Li, J.J., Cesaroni, R., Sanna, A., Xu, Y., & Zhang, Q. 2013, A&A, 549, A122

Mottram, J.C., Hoare, M.G., Urquhart, J.S., et al. 2011a, A&A, 525, A149

Mottram, J.C., Hoare, M.G., Davies, B., et al. 2011b, ApJ, 730, L33

Murillo, N.M., Lai, S.-P., Bruderer, S., Harsono, D., van Dishoeck, E.F. 2013, A&A, 560, 103

Ossenkopf, V. & Henning, Th. 1994, A&A, 291, 943

Peters, T., Banerjee, R., Klessen, R.S., et al. 2010, ApJ, 711, 1017

Peters, T., Banerjee, R., Klessen, R.S., & Mac Low, M.-M. 2011, ApJ, 729, 72

Peters, T., Klaassen, P.D., Mac Low, M.-M., et al. 2014, ApJ, 788, 14

Rosen, A.L., Krumholz, M.R., & Ramirez-Ruiz, E. 2012, ApJ, 748, 97

Sánchez-Monge, Á., Cesaroni, R., Beltrán, M.T., et al. 2013, A&A, 552, L10

Sánchez-Monge, Á., Beltrán, M.T., Cesaroni, R., et al. 2014, A&A, 569, A11

Sánchez-Monge, Á., Schilke, P., Ginzburg, A., Cesaroni, R., & Schmiedeke, A. 2017, A&A, submitted

Schuller, F., Menten, K.M., Contreras, Y., et al. 2009, A&A, 504, 415

Sollins, P.K., Hunter, T.R., Battat, J., et al. 2004, ApJ, 616, L35

Tan, J.C., Beltrán, M.T., Caselli, P., et al. 2014, in Protostars and Planets VI, ed. H. Beuther, R. S. Klessen, C. P. Dullemond, and T. Henning (Tucson: Univ. of Arizona Press), 149

Tobin, J.J., Looney, L.W., Wilner, D.J., et al. 2015, ApJ, 805, 125

Urquhart, J.S., Busfield, A.L.. Hoare, M.G., et al. 2008, A&A, 487, 253

Urquhart, J.S., Hoare, M.G., Purcell, C.R., et al. 2009, A&A, 501, 539

Vacca, W.D., Garmany, C.D., & Shull, M. 1996, ApJ, 460, 914

van der Tak, F.F.S., van Dishoeck, E.F., Evans, N.J., II, Blake, G.A. 2000, ApJ, 537, 283

Vig, S., Cesaroni, R., Testi, L., Beltrán, M.T., & Codella, C. 2008, A&A, 488, 605

Zapata, L.A., Palau, A., Galván-Madrid, R., et al. 2015, MNRAS, 447, 1826

Zhang, B., Moscadelli, L., Sato, M., Reid, M.J., et al. 2014, ApJ, 781, 89

Zhang, Y., Tan, J.C., De Buizer, J.M., et al. 2013, ApJ, 767, 58